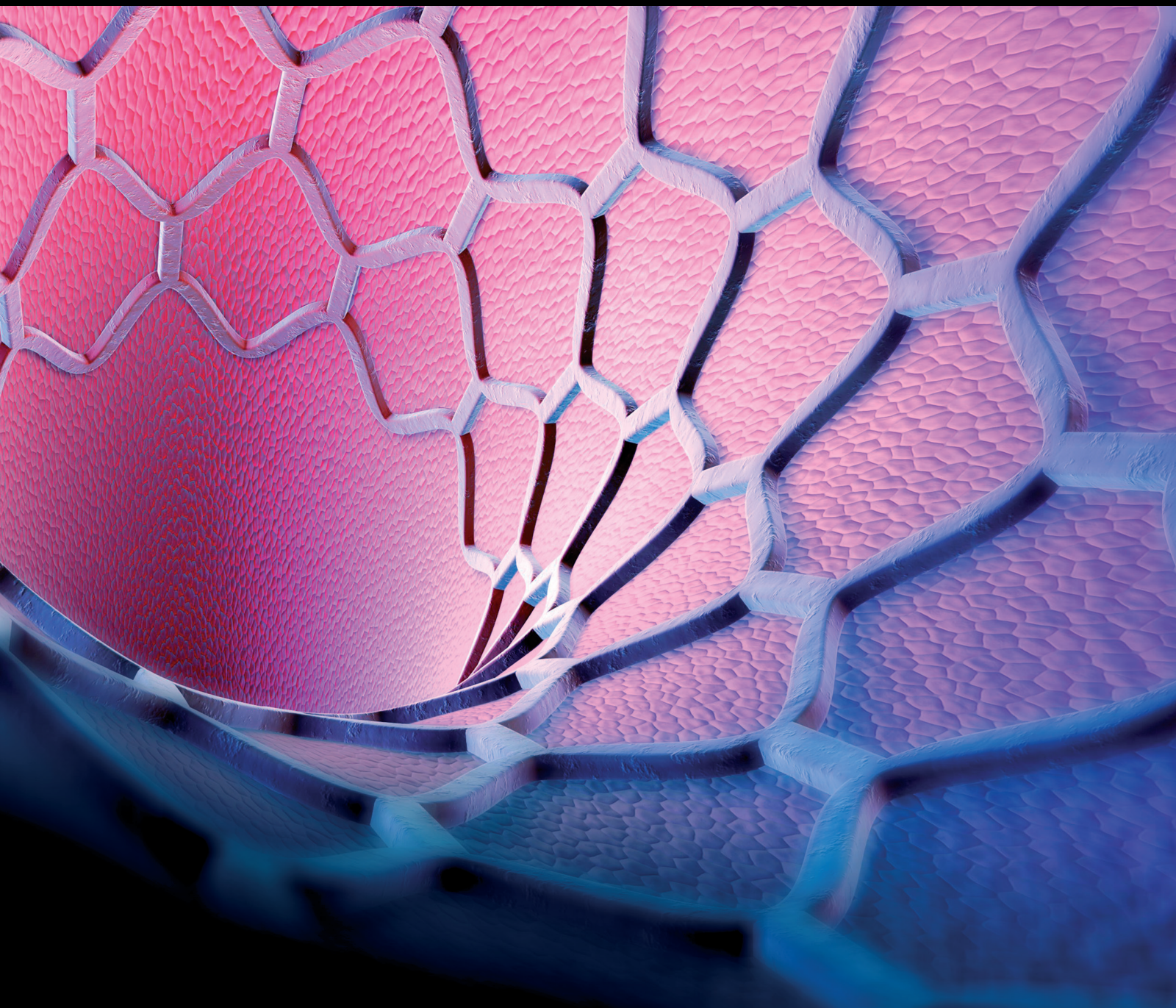


Artificial Intelligence in Structural Heart Disease

Lead Guest Editor: Verena Veulemans

Guest Editors: Matti Adam, Nicolas Van Mieghem, and Ole De Backer





Artificial Intelligence in Structural Heart Disease

Journal of Interventional Cardiology

Artificial Intelligence in Structural Heart Disease

Lead Guest Editor: Verena Veulemans

Guest Editors: Matti Adam, Nicolas Van Mieghem,
and Ole De Backer



Copyright © 2022 Hindawi Limited. All rights reserved.

This is a special issue published in "Journal of Interventional Cardiology." All articles are open access articles distributed under the Creative Commons Attribution License, which permits unrestricted use, distribution, and reproduction in any medium, provided the original work is properly cited.

Chief Editor

Patrizia Presbitero, Italy

Academic Editors

Amr E. Abbas, USA
Antonio Abbate, USA
Jeremiah Brown , USA
Fausto Castriota, Italy
Periklis Davlourous, Greece
Leonardo De Luca , Italy
Salvatore De Rosa , Italy
Seif S. El-Jack, New Zealand
Anca Daniela Farcas , Romania
Gopal Chandra Ghosh , India
Cristina Giannini, Italy
Akshay Goel , USA
Runmin Guo, China
William B. Hillegass , USA
Yu-Li Huang , China
David G. Iosseliani , Russia
Adam Kern , Poland
Michael C. Kim, USA
Faisal Latif, USA
Michael Lichtenauer , Austria
Yuichiro Maekawa , Japan
Benedetta Maria Motta , Italy
Piotr Musiafek, Poland
Toshiko Nakai , Japan
Thach N. Nguyen , USA
Vasileios Panoulas , United Kingdom
Stefano Rigattieri , Italy
Kintur Sanghvi, USA
Celestino Sardu , Italy
Alessandro Sciahbasi, Italy
Fernando Scudiero , Italy
Magnus Settergren, Sweden
Martin J. Swaans , The Netherlands
Jan-Peter Van Kuijk, The Netherlands
Luigi Vignali, Italy
Ming-Ming Wu , China
Zhen Yang , China
Shenghua Zhou , China

Contents

Automated MSCT Analysis for Planning Left Atrial Appendage Occlusion Using Artificial Intelligence

Kilian Michiels , Eva Heffinck , Patricio Astudillo , Ivan Wong , Peter Mortier, and Alessandra Maria Bavo 

Research Article (9 pages), Article ID 5797431, Volume 2022 (2022)

Artificial Intelligence Enabled Fully Automated CMR Function Quantification for Optimized Risk Stratification in Patients Undergoing Transcatheter Aortic Valve Replacement

Ruben Evertz , Torben Lange , Sören J. Backhaus , Alexander Schulz, Bo Eric Beuthner, Rodi Topci , Karl Toischer, Miriam Puls, Johannes T. Kowallick, Gerd Hasenfuß, and Andreas Schuster 

Research Article (9 pages), Article ID 1368878, Volume 2022 (2022)

Joint Analysis of Morphological Parameters and In Silico Haemodynamics of the Left Atrial Appendage for Thrombogenic Risk Assessment

Maria Isabel Pons, Jordi Mill , Alvaro Fernandez-Quilez , Andy L. Olivares , Etelvino Silva, Tom de Potter, and Oscar Camara 

Research Article (10 pages), Article ID 9125224, Volume 2022 (2022)

Research Article

Automated MSCT Analysis for Planning Left Atrial Appendage Occlusion Using Artificial Intelligence

Kilian Michiels ¹, Eva Heffinck ¹, Patricio Astudillo ¹, Ivan Wong ², Peter Mortier,¹
and Alessandra Maria Bavo ¹

¹FEops NV, Gent, Belgium

²The Heart Centre, Rigshospitalet, Copenhagen University Hospital, Copenhagen, Denmark

Correspondence should be addressed to Alessandra Maria Bavo; alessandra.bavo@feops.com

Received 21 December 2021; Accepted 29 March 2022; Published 27 April 2022

Academic Editor: Matti Adam

Copyright © 2022 Kilian Michiels et al. This is an open access article distributed under the Creative Commons Attribution License, which permits unrestricted use, distribution, and reproduction in any medium, provided the original work is properly cited.

Background. The number of multislice computed tomography (MSCT) analyses performed for planning structural heart interventions is rapidly increasing. Further automation is required to save time, increase standardization, and reduce the learning curve. **Objective.** The purpose of this study was to investigate the feasibility of a fully automated artificial intelligence (AI)-based MSCT analysis for planning structural heart interventions, focusing on left atrial appendage occlusion (LAAO) as the selected use case. **Methods.** Different deep learning models were trained, validated, and tested using a cohort of 583 patients for which manually annotated data were available. These models were used independently or in combination to detect the anatomical ostium, the landing zone, the mitral valve annulus, and the fossa ovalis and to segment the left atrium (LA) and left atrial appendage (LAA). The accuracy of the models was evaluated through comparison with the manually annotated data. **Results.** The automated analysis was performed on 25 randomly selected patients of the test cohort. The results were compared to the manually identified landmarks. The predicted segmentation of the LA(A) was similar to the manual segmentation (dice score of 0.94 ± 0.02). The difference between the automatically predicted and manually measured perimeter-based diameter was -0.8 ± 1.3 mm (anatomical ostium), -1.0 ± 1.5 mm (Amulet landing zone), and -0.1 ± 1.3 mm (Watchman FLX landing zone), which is similar to the operator variability on these measurements. Finally, the detected mitral valve annulus and fossa ovalis were close to the manual detection of these landmarks, as shown by the Hausdorff distance (3.9 ± 1.2 mm and 4.8 ± 1.8 mm, respectively). The average runtime of the complete workflow, including data pre- and postprocessing, was 57.5 ± 34.5 seconds. **Conclusions.** A fast and accurate AI-based workflow is proposed to automatically analyze MSCT images for planning LAAO. The approach, which can be easily extended toward other structural heart interventions, may help to handle the rapidly increasing volumes of patients.

1. Introduction

During the last decade, there has been an exponential growth in the number of structural heart interventions, largely driven by the widespread adoption of transcatheter aortic valve replacement (TAVR) [1]. A continued growth can be expected in the coming years due to a further expansion of TAVR in combination to significantly increase volumes for several other interventions, such as left atrial appendage occlusion (LAAO) and transcatheter mitral valve repair and replacement (TMVR).

Medical imaging is of utmost importance for all these structural heart interventions, from preprocedural planning to intraprocedural guidance and postprocedural follow-up. A wide variety of imaging modalities can be used during these different stages. Notably, many centers rely on multislice computed tomography (MSCT) for preprocedural planning [2, 3]. Driven by the enormous growth in structural heart interventions, there has been a steep increase in the number of MSCT analyses that need to be performed. Given that the currently available software solutions only provide semi-automated workflows, further automation is required.

This may not only help to save a considerable amount of time but can also result in more standardization and a shorter learning curve for a starting operator.

An MSCT analysis for planning structural heart interventions—whether this is TAVR, LAAO, or any other procedure—typically requires identifying certain anatomical landmarks and deriving measurements from these landmarks, in order to assess the procedural risks and to guide device selection and sizing. In addition, a segmentation or 3D volume reconstruction of certain anatomical structures is sometimes performed to better understand the patient's anatomy. With the recent advances in artificial intelligence (AI), it has become possible to automate all these tasks (landmark identification, measurements, and 3D reconstruction) [4, 5].

The aim of this study was to investigate the feasibility of a fully automated AI-based MSCT analysis for planning structural heart interventions, focusing on LAAO as the selected use case.

2. Methods

This retrospective study was performed using MSCT images acquired for the preoperative planning of the LAAO. The full cohort contains 583 distinct MSCT datasets collected from 41 different medical centers. The patient cohort is characterized by a mean age of 76.5 ± 7.9 years, and 44.9% of male and 24.7% of female patients (gender unknown in 30.4% of the patients).

2.1. MSCT Analysis for LAAO in Clinical Practice. A typical MSCT analysis for the preprocedural planning of LAAO involves several aspects [3, 6]. The size of the left atrial appendage (LAA) is assessed by identifying the 3D planes defining the entrance of the LAA (i.e., anatomical ostium) and a device-specific landing zone, and by performing measurements in these planes. The depth of the appendage is also measured, to understand whether the LAA is deep enough to host the selected device. To plan the transseptal puncture site, the fossa ovalis is identified as a 3D curve on the interatrial septum. Locating the mitral valve annulus can also be useful to assess whether there could be any potential interaction between the implanted occluder and the mitral valve. Finally, a 3D model reconstruction of the left atrium (LA) and the LAA is often generated through image segmentation techniques to better understand the patient's anatomy. The described anatomical landmarks and measurements are depicted together with the 3D model of the LA(A) in Figure 1.

2.2. Manual MSCT Analysis Available as Ground Truth. Manually annotated or “ground truth” data have been produced by trained professionals for all the above-mentioned landmarks and the 3D segmentation of the LA(A), using the Materialise Mimics Innovation Suite 21 (Materialise, Leuven, Belgium), according to the indications provided in the instruction for use of the devices and in the most relevant literature of the field [3]. Not all annotations

are available for all patients as some were added at a later stage of the study.

For 25 patients, three trained professionals identified the ostium and landing zone planes independently and performed the related measurements. This provides interoperator variability data that allow to correctly interpret the accuracy of the deep learning models.

2.3. Automated MSCT Analysis. Four distinct application types based on deep learning are used independently or in combination to provide the required output for the anatomical analysis: segmentation, point detection, curve detection, and plane detection. The complete data flow, starting from the resampled MSCT data, is shown in Figure 2. The deep learning models used here are based on the NiftyNet implementation [6] (variations of DenseVNet [5]), where the prior and the initial average pooling layer can be omitted. Other strategies were investigated, but none gave comparable results in terms of accuracy.

For each application, the amount of data used for the training, validation, and testing of the deep learning models was 80%, 10%, and 10%, respectively. Data were randomly distributed over these three different groups.

The train and validate set are used during the training and hyperparameter optimization of the deep learning models, while the test set is an “unseen” dataset used to assess model accuracy. For the purpose of this manuscript, a fixed group of 25 randomly selected patients was used in the test cohort for all applications. The average age in this test set is 77.35 ± 8.22 years. The gender distribution is 52% of male patients, 16% of female patients, and 32% of unknown patients. For the same 25 patients, the manual annotations obtained from different operators were used in the interoperator variability study to assess the accuracy of the automated ostium and landing zone plane detection and the related anatomical measurements. This condition does not alter the data distribution across the groups, but it ensures a meaningful comparison of the results.

In order to automatically perform the above-described anatomical analysis for LAAO, a preprocessing step of the MSCT data is required. Initially, one cardiac phase has to be selected. This step is performed manually, and it is not included in the “automatic analysis workflow” described here. As part of the automatic process, firstly the MSCT volume needs to be resampled to an isotropic resolution and voxel size (different values depending on the specific application). Once the MSCT volumes are isotropic, they are resized or cropped to an application-specific input shape. The difference between resizing and cropping is illustrated in Figure 3.

The following sections provide more details regarding the four different types of applications.

2.3.1. Segmentation. Segmentation is the task of assigning a specific label to each part of the input. In this case, the input is a 3D volume and the segmentation output is a 3D volume of the same shape, with a label identifier assigned to each voxel inside the volume. The manually obtained segmentation

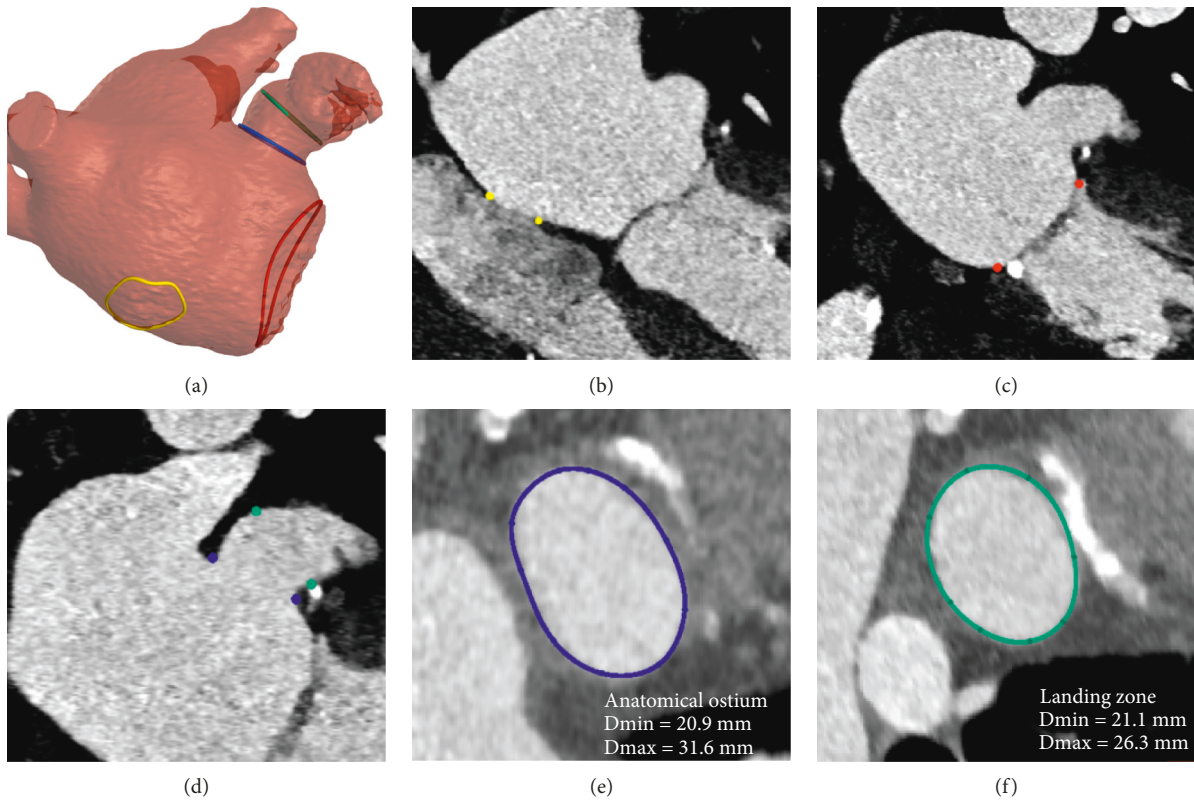


FIGURE 1: Anatomical structures and landmarks identified by the model. (a) 3D model reconstructed from the segmentation of the left atrium and left atrial appendage, where the landmarks of the anatomical ostium (blue), landing zone (green), fossa ovalis (yellow), and mitral annulus (red) are reported. (b) Fossa ovalis region indicated on the DICOM (yellow). (c) Mitral annulus indicated on the DICOM (red). (d) Anatomical ostium and landing zone indicated on the DICOM (blue and green, respectively). (e) Anatomical ostium plane. (f) Landing zone plane (Amulet device).

masks describe which voxels are part of the LA(A), and these data are used to train a deep learning model. An example of the LA(A) mask is shown in Figure 4(a). When applying the trained deep learning model, a probability mask is returned, describing the probability that a certain voxel belongs to the LA(A) label. Postprocessing of the model output is required to binarize the obtained probability mask. Given a threshold, all probabilities in the mask below this threshold are set to label zero, while all values equal to or higher than the threshold are set to label one. The resulting segmentation mask is the volume described by all the voxels with label one. To obtain a higher precision mask, the deep learning mask is combined with masks obtained through image analysis techniques (such as water shedding).

2.3.2. Point Detection. In order to detect a 3D point within the MSCT volume, the location of the manually identified point is used to generate a segmentation mask by assigning a predefined label to a spherical region around the point (highlighted in dark red in Figure 4(b)). Deep learning models are then trained to return a probability mask of that same region. Postprocessing is similar as compared to the segmentation application, with the additional step of taking the centroid of all the similar labels to obtain a 3D point. This 3D point detection is used to identify specific regions of interest

in the MSCT data for further processing as shown in Figure 2. For example, the centroid of the mitral valve is detected in order to crop the MSCT data around the mitral valve, which is then used to identify the mitral valve annulus. This application type is based on the work of Astudillo et al. [8].

2.3.3. Curve Detection. The manually identified curves (fossa ovalis or mitral annulus) are used to generate a segmentation mask by sweeping a sphere along the curve with an application-dependent radius. This results in a torus-shaped segmentation mask (Figure 4(c)). The probability mask returned by a trained deep learning model is transformed into a 3D curve using graph-based techniques, as described in the work of Astudillo et al. [9].

2.3.4. Plane Detection. Plane detection is fundamental to derive the diameter measurements used by physicians to understand the size of the LAA. The manually identified planes (such as the anatomical ostium and landing zone) are used to split the manually obtained LA(A) segmentation mask into two regions, as shown in Figure 4(d). Using this input, deep learning models are trained to assign voxels within the LA(A) to one of these two labels. Subsequently, the connecting boundary between the voxels annotated by

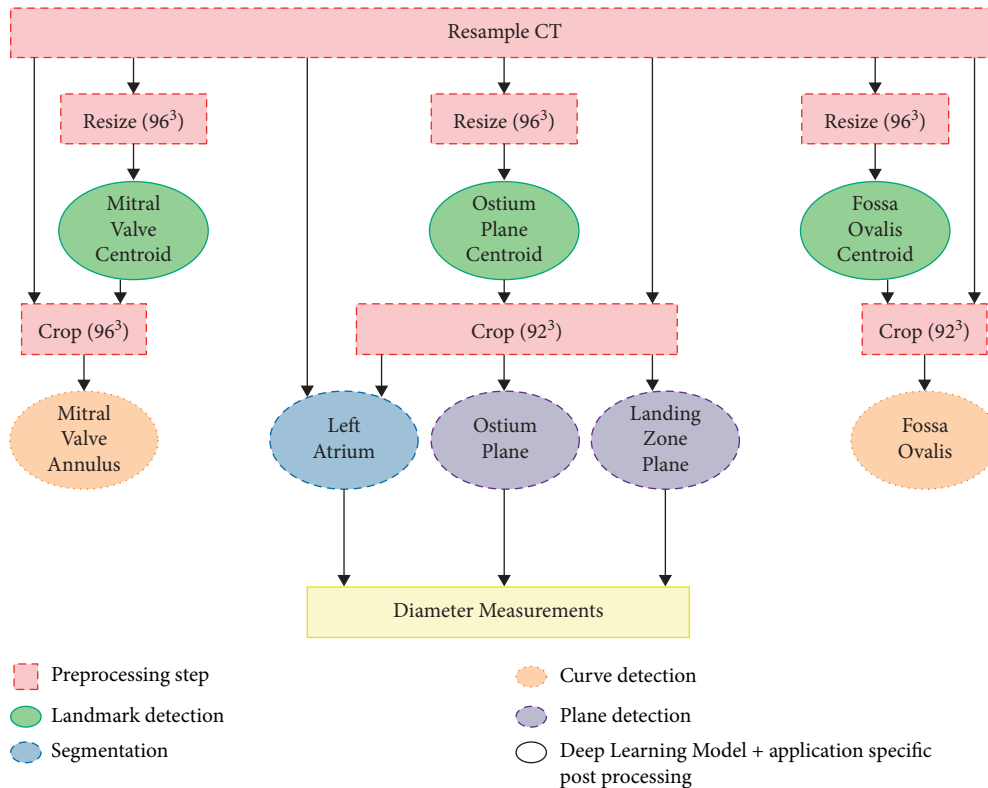


FIGURE 2: Overview of the steps included in the complete workflow.

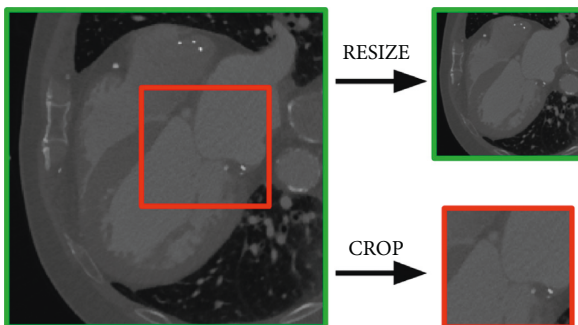


FIGURE 3: CT data can be resized (top right) or cropped (bottom right) depending on the application at hand. Resizing keeps the entire data but in a smaller format. Cropping takes out a region of interest without any resizing.

these labels can be extracted using imaging processing techniques and used to fit a plane.

2.4. Derived Measurements. Using the items described above, additional output required for the preoperative planning can be extracted. For each of the detected planes (ostium and landing zones), a closed curve describing the boundary of the appendage in the predicted planes is derived using the LA(A) segmentation and four diameters are calculated (area-based, perimeter-based, minimum, and maximum diameters).

The LAA depth (for Amulet devices) can also be derived, calculated as the distance between the centroid of the

anatomical ostium plane and its projection to the LAA surface, at the roof of the LAA. With a similar procedure, the LAA depth (for Watchman FLX devices) can be derived, by calculating the distance between the landing zone centroid and the LAA tip.

2.5. Evaluation Metrics. Depending on the application, the prediction is evaluated using different metrics. Segmentations are evaluated by the Sørensen–Dice coefficient [10, 11], while for point detections, the Euclidean distance between the predicted and ground truth curves is used.

The curve detection models are assessed with the Euclidean distance between the centroids of the predicted and ground truth curves. This metric provides information about the accuracy of the location of the detected curve. In addition, the Hausdorff distance [12] and the difference in diameter of the predicted and ground truth curves are calculated to assess the accuracy of the shape of the curve.

The detected planes are evaluated using the angle between the predicted and ground truth planes. In addition, the Euclidean distance between the centroid of the closed curve describing the boundary of the appendage in the predicted and ground truth planes is calculated to assess the location error.

2.6. Quality Control. For the purpose of this manuscript, the results reported in the following sections do not include any quality check step or manual modifications, to ensure that the accuracy of the models is calculated without any subjective corrective action. The processing time reported refers

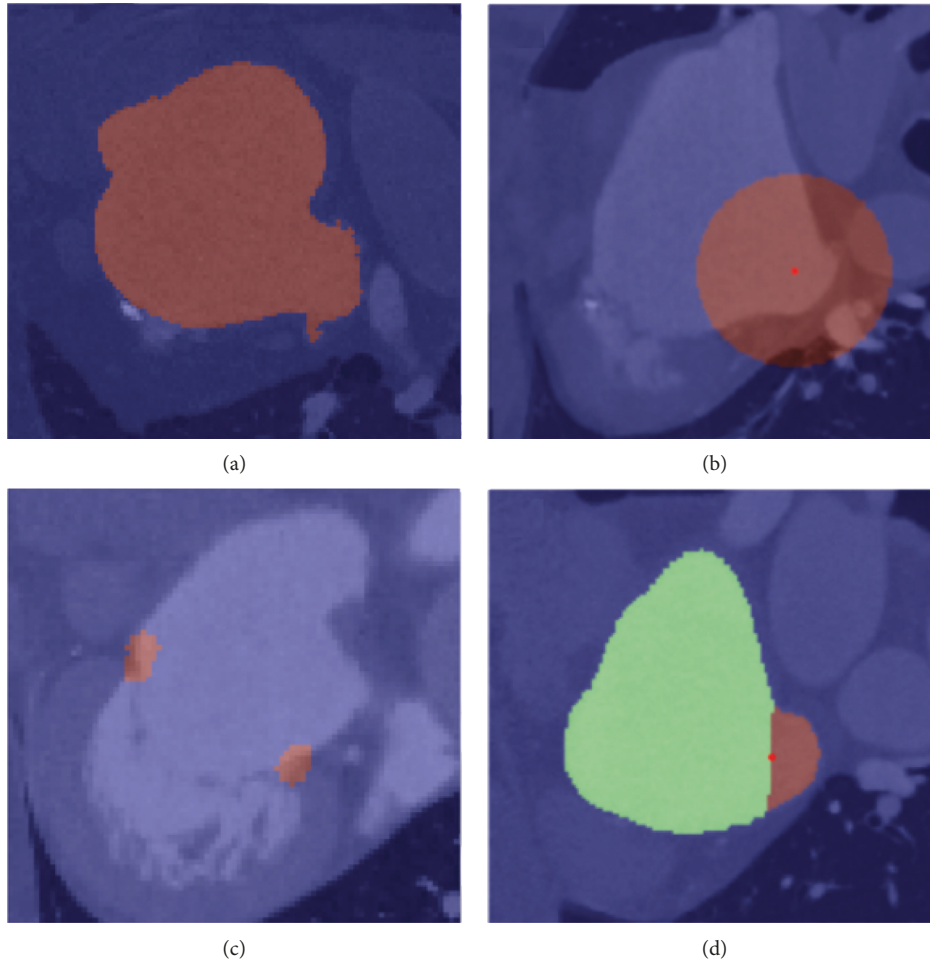


FIGURE 4: Different ground truth masks created for the AI model trainings, overlaid on top of the DICOM images. (a) Segmentation of the left atrium and left atrial appendage. (b) Point detection, where the dark red region (label) represents the spherical region around the point, and the bright red dot is the centroid of the mask identified as output. (c) 3D curve detection. (d) Plane detection, where the different labels are identified with different colors.

to the automatic tasks only, even though manual steps (e.g., phase selection) are still required in the preprocessing phase.

3. Results

The automated analysis was completed for the patients included in the test cohorts ($n = 25$). The average runtime of the complete workflow, including data pre- and post-processing, was 57.5 ± 34.5 seconds when executed on a GPU server with 4 GPUs (2x Nvidia GeForce RTX 2080 ti, 1x Nvidia GeForce RTX 2070 SUPER, and 1x GeForce GTX TITAN X) and 64 GB RAM, using TorchServe [13]. The time spent by qualified professionals to perform the same tasks manually was approximately 10–15 minutes per patient.

The accuracy of the different applications is provided in the following paragraphs. For each patient, the comparison between the automatic and the manual analyses has been performed on images of the same cardiac phase.

3.1. LA(A) Segmentation. The mask resulting from the deep learning models and the image analysis techniques is evaluated

for the 25 patients on whom the interoperator variability study was performed. The mean Dice score is 0.94 ± 0.02 .

3.2. Plane Detections and Related Measurements. The prediction of the anatomical ostium and landing zone planes, as well as the resulting anatomical measurements, is evaluated using the interoperator variability data that were conducted on 25 patients. Table 1 provides an overview of all the results using the data from observer 1 as the comparator. It can be observed that the differences between the model predictions and observer 1 are very similar to the differences between the different observers, both in terms of the derived measurements as well as for the location and orientation of the detected planes. Scatter and Bland–Altman plots are provided in Figure 5 for the perimeter-based diameter at the ostium and the different landing zone planes. Figure 6 shows the manually identified and predicted curves for one randomly selected patient.

3.3. Mitral Valve Annulus. The mean diameter difference of the detected mitral valve annulus is 0.1 ± 0.9 mm for the test set, while the mean Hausdorff distance is 3.9 ± 1.2 mm. This

TABLE 1: Overview of the differences between the manual analysis from observer 1 (obs1), the model predictions, and the manual analyses of observer 2 (obs2) and 3 (obs3). The differences are reported as mean \pm standard deviation.

	Model vs. obs1	Obs2 vs. obs1	Obs3 vs. obs1
Anatomical ostium plane			
Area-based diameter (mm)	-0.8 ± 1.3	-0.8 ± 1.2	-0.4 ± 1.1
Perimeter-based diameter (mm)	-0.8 ± 1.3	-0.8 ± 1.3	-0.4 ± 1.2
Maximal diameter (mm)	-0.9 ± 2.0	-0.9 ± 1.6	-0.6 ± 1.6
Minimal diameter (mm)	-0.6 ± 1.1	-0.6 ± 1.1	-0.1 ± 0.8
Centroid (mm)	1.9 ± 1.0	1.9 ± 0.9	1.7 ± 0.7
Angle [°]	6.5 ± 2.9	6.0 ± 3.0	6.5 ± 3.4
Landing zone plane (amulet)			
Area-based diameter (mm)	-0.9 ± 1.5	-0.2 ± 0.6	0.3 ± 1.0
Perimeter-based diameter (mm)	-1.0 ± 1.5	-0.2 ± 0.6	0.3 ± 1.0
Maximal diameter (mm)	-1.2 ± 2.0	-0.4 ± 1.1	0.2 ± 1.3
Minimal diameter (mm)	-0.6 ± 1.7	0.0 ± 0.9	0.6 ± 0.9
Centroid (mm)	1.8 ± 1.1	1.7 ± 0.9	1.5 ± 0.8
Angle [°]	8.3 ± 5.1	6.6 ± 3.7	8.9 ± 3.6
Landing zone plane (Watchman FLX)			
Area-based diameter (mm)	-0.1 ± 1.2	0.2 ± 1.0	0.7 ± 0.9
Perimeter-based diameter (mm)	-0.1 ± 1.3	0.1 ± 1.1	0.8 ± 1.0
Maximal diameter (mm)	0.1 ± 1.7	0.2 ± 1.9	0.9 ± 1.5
Minimal diameter (mm)	-0.2 ± 1.4	0.0 ± 0.9	0.6 ± 1.0
Centroid (mm)	1.8 ± 1.5	2.0 ± 1.3	2.0 ± 1.0
Angle [°]	7.8 ± 5.1	7.7 ± 4.7	8.4 ± 4.9

means that the shape of the predicted mitral valve annulus is accurately predicted. The location error is represented by the mean distance error between the ground truth and the centroids of the predicted curve. This error is 1.2 ± 0.8 mm and confirms the location accuracy of the predicted curve. Figure 7 shows a qualitative comparison of the predicted and ground truth mitral annulus curves for nine randomly selected patients included in the test set.

3.4. Fossa Ovalis. For the test set, the fossa ovalis mean diameter difference is -2.7 ± 4.2 mm, with a Hausdorff distance of 6.7 ± 5.1 mm. The Euclidean distance error on the centroid of the curve is 4.1 ± 5.0 mm. Of note, the region of the fossa ovalis is clearly visible only if there is sufficient contrast filling in the right atrium. The MSCT acquisition protocols vary from center to center, and not for all patients the contrast sufficiently reaches the right atrium for the identification of a proper fossa ovalis. This explains why for the fossa ovalis the performance of the model is lower than for the mitral annulus. When excluding from the analysis the 4 DICOM datasets with poor contrast filling in the right heart, the mean diameter difference is reduced to -2.1 ± 3.0 mm, with a Hausdorff distance of 4.8 ± 1.4 mm. The Euclidean distance error on the centroid of the curve is 2.3 ± 1.0 mm.

In Figure 8, a qualitative comparison of the prediction and the ground truth is given for nine patients randomly selected from the test set.

4. Discussion

4.1. Preoperative LAAO Anatomical Analysis Tool. Several AI-powered models have been reported in the literature [14, 15], and tools and platforms are described offering

semi-automated analysis, based on 3D echocardiography [16] and MSCT images [17]. Commercially available software exists, allowing for a predefined workflow for the preoperative planning of LAAO procedures, where the physician still needs to interact with the tool and provide manual input to the software.

In this work, we presented a framework consisting of several AI-based applications, to allow for the automatic anatomical analysis needed for the preoperative planning of the LAAO. After the preprocessing phase to ensure image selection and standardization, no interaction or input is required to generate the results. The proposed method is based on MSCT scans, which provide high spatial resolution. The availability of larger portions of the heart compared to 3D echocardiography allows the inclusion of relevant structures such as the fossa ovalis contour, for transseptal puncture planning. The proposed method is independent from the origin of the data, MSCT machinery manufacturers, and MSCT acquisition protocol, as the model has been developed and tested on a large database spanning a wide range of parameters for the abovementioned characteristics.

The presented framework is fast (1 minute vs. 10–15 minutes of manual work), accurate, and is built on a large database (>500 MSCT scans), providing a solid base for the AI-based models. This framework can easily be extended to other structural heart disease interventions. The availability of such an analysis for physicians ensures a fast and accurate anatomical analysis, which is crucial for a successful and efficient LAAO procedure.

Clinically, as the LAAO procedure is still not as widespread as TAVR, the learning curve of preprocedural planning in low-volume centers can be long and difficult. The availability of an automatic tool for the preoperative anatomical analysis may not only result in more

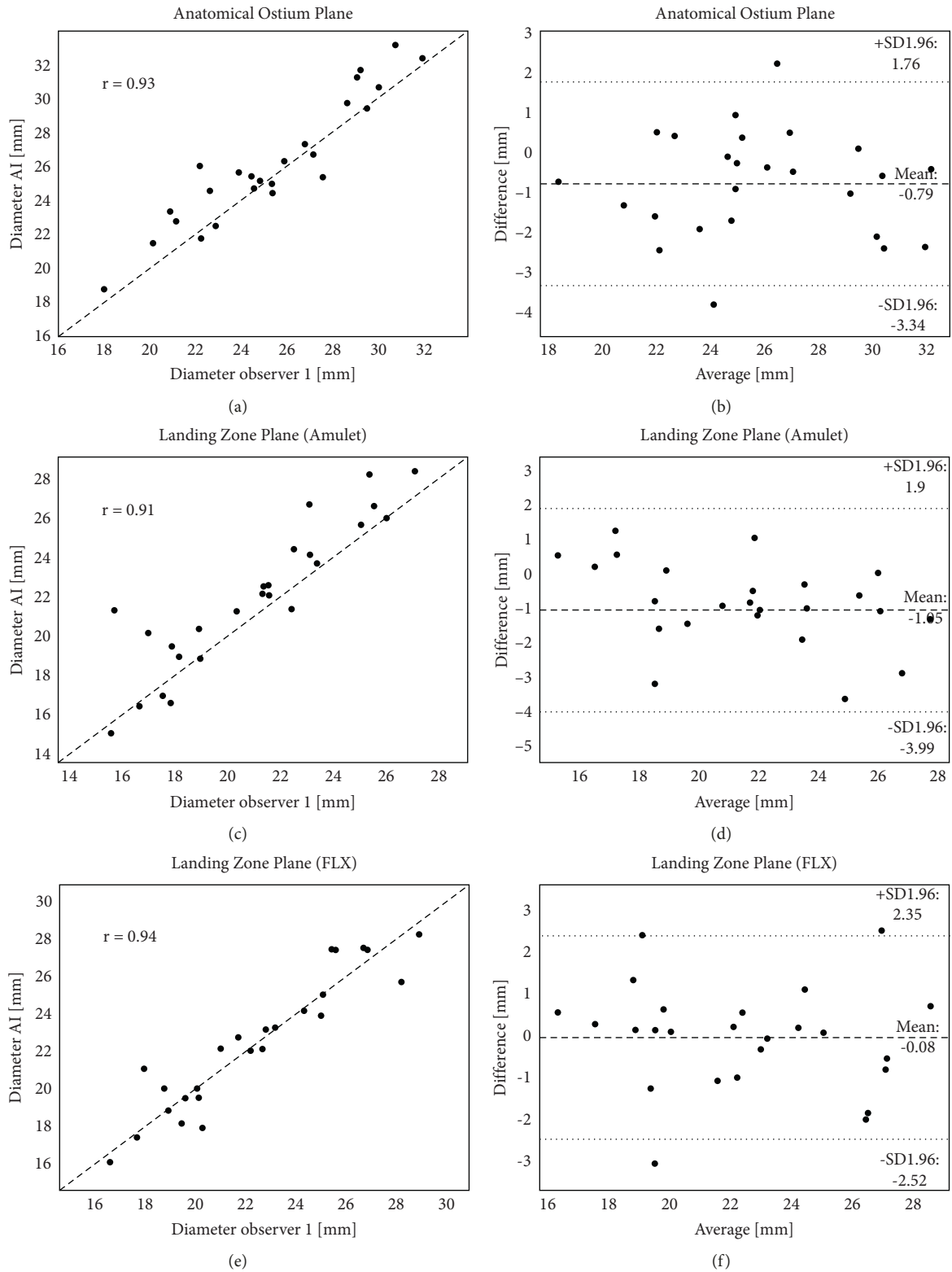


FIGURE 5: Overview of the results obtained for the comparison between the AI models and one of the manually identified measurements. All graphs report the results obtained for the perimeter-based diameter of the indicated cross-section (a-b: anatomical ostium, c-d: landing zone Amulet, e-f: landing zone Watchman FLX). Graphs (a-c-e) scatter plot with R Pearson coefficient. Graphs (b-d-f) Bland-Altman analysis with mean value and limits of agreement.

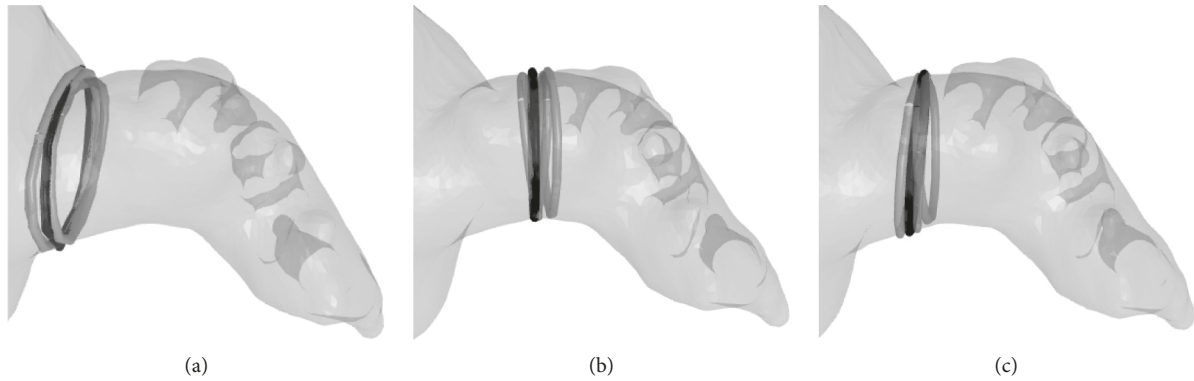


FIGURE 6: Example of the ostium and landing zone curves in the detected planes for 1 patient. The black curve shows the predicted curve, while the curves from the three different observers are shown in gray. (a) Anatomical ostium plane. (b) Landing zone plane (Amulet). (c) Landing zone plane (Watchman FLX).



FIGURE 7: Mitral valve annulus curves for nine randomly selected patients of the test dataset. The manually detected and the predicted curve are displayed in gray and black, respectively.

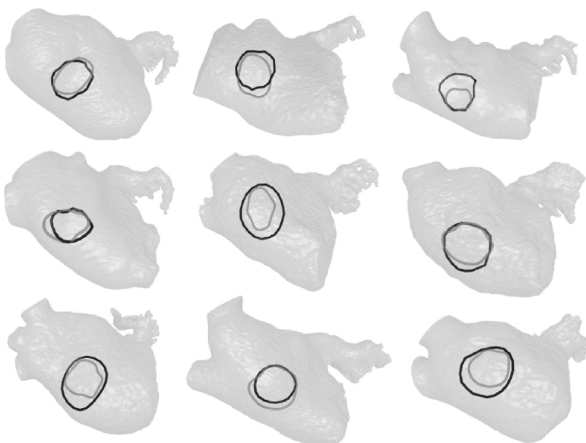


FIGURE 8: Fossa ovalis curves for nine randomly selected patients from the test dataset. The manually detected and the predicted curve are displayed in gray and black, respectively.

standardization across different operators but may also shorten the learning curve during initiation of the programs.

4.2. Quality Control and User Interaction. As stated before, all the results presented here are calculated in a fully automated manner, to prove the accuracy of the models. When the

applications described are translated into clinical practice tools, the interaction with the user or the physician remains fundamental. As the preoperative planning of a procedure relies on the extensive experience of the operator, it is the authors' vision that the physician should always be able to interact with the provided results, and to modify them if needed. For example, a way to deliver the AI results would be the inclusion of the described models into a user-friendly interface, where the operator can inspect, review, and modify the preoperative landmarks and measurements if needed.

Furthermore, to ensure the applicability of the developed methodology regardless of infrastructure limitations, such a model could be integrated into a cloud-based service/platform, which is easily accessible and removes several constraints on hardware availability and maintenance.

4.3. Extension to Other Fields of Application. The work presented for LAAO preprocedural planning serves as a use case to demonstrate the availability, accuracy, and speed of the developed AI-based applications. Additional features to the workflow can be easily integrated, to expand the preoperative planning even further. Relevant additions are the LAA centerline detection, to understand the tortuosity of anatomies and the positioning of the delivery system; to investigate the trajectory between the transseptal puncture location and the access to the LAA, and computational simulations [18]; and to calculate the physical interaction between the virtually deployed device and the anatomical structures.

Similar algorithms can be used for other interventions, where preoperative planning of transcatheter procedures based on MSCT images is mandatory. For TAVR, this may be very useful considering the large number of MSCT analyses that need to be performed in high-volume centers [4]. It also has the potential to significantly speed up the planning of procedures such as TMVR, where multiple analyses at different phases of the cardiac cycle are required, resulting in a relatively time-consuming process [7, 9].

4.4. Current Limitations. The current study logically has some limitations. The interoperator variability study conducted as a comparator included only a limited cohort of

patients ($n = 25$). For a stronger comparison and dedicated statistical subanalyses to detect potential patterns in the automated landmark detection, a larger cohort of patients should be analyzed by qualified operators.

From a clinical point of view, the models have been presented and validated for the LAAO use case. The extension to other structural heart interventions might require the implementation of additional models, to deliver all the relevant landmarks and parameters necessary for the planning of the corresponding procedures.

5. Conclusion

This manuscript presents a fast and accurate AI-based workflow, to automatically analyze MSCT images for pre-procedural planning of LAAO interventions. The approach, which can be easily extended to other structural heart interventions, may help to handle the rapidly increasing volumes of patients, to speed up the manual process of anatomical analysis, and to facilitate the preoperative planning for transcatheter procedures.

Data Availability

The statistical data used to support the findings of this study are available from the corresponding author upon request.

Conflicts of Interest

PM is a shareholder of FEops, and KM, EH, PA, and AB are employees of FEops. IW has no conflicts of interest to declare.

Authors' Contributions

The authors Kilian Michiels and Eva Heffinck contributed equally to the manuscript.

Acknowledgments

This study is part of a project that has received funding from the European Union's Horizon 2020 research and innovation program under grant agreement no. 945698.

References

- [1] J. D. Carroll, M. J. Mack, S. Vemulapalli et al., "STS-ACC TVT registry of transcatheter aortic valve replacement," *Journal of the American College of Cardiology*, vol. 76, no. 21, pp. 2492–2516, 2020.
- [2] P. Blanke, J. R. Weir-McCall, S. Achenbach et al., "Computed tomography imaging in the context of transcatheter aortic valve implantation (TAVI)/Transcatheter aortic valve replacement (TAVR)," *Journal of the American College of Cardiology: Cardiovascular Imaging*, vol. 12, no. 1, pp. 1–24, 2019.
- [3] K. Korsholm, S. Berti, X. Iriart et al., "Expert recommendations on cardiac computed tomography for planning transcatheter left atrial appendage occlusion," *JACC: Cardiovascular Interventions*, vol. 13, no. 3, pp. 277–292, 2020.
- [4] P. Astudillo, P. Mortier, J. Bosmans et al., "Enabling automated device size selection for transcatheter aortic valve implantation," *Journal of Interventional Cardiology*, vol. 2019, 7 pages, Article ID 3591314, 2019.
- [5] E. Gibson, F. Giganti, Y. Hu et al., "Automatic multi-organ segmentation on abdominal CT with dense V-networks," *IEEE Transactions on Medical Imaging*, vol. 37, no. 8, pp. 1822–1834, 2018.
- [6] E. Gibson, W. Li, C. Sudre et al., "NiftyNet: a deep-learning platform for medical imaging, Computer Methods and Programs in Biomedicine," vol. 158, 2018 https://github.com/NifTK/NiftyNet/blob/dev/niftnet/network/dense_vnet.py.
- [7] M. Glikson, R. Wolff, G. Hindricks et al., "EHRA/EAPCI expert consensus statement on catheter-based left atrial appendage occlusion - an update," *EP Europace*, vol. 22, no. 2, 184 pages, 2020.
- [8] P. Astudillo, P. Mortier, J. Bosmans et al., "Automatic detection of the aortic annular plane and coronary ostia from multidetector computed tomography," *Journal of Interventional Cardiology*, vol. 2020, 9 pages, Article ID 9843275, 2020.
- [9] P. Astudillo, M. De Beule, J. Dambre, and P. Mortier, "Towards safe and efficient preoperative planning of transcatheter mitral valve interventions," *Morphologie*, vol. 103, no. 343, pp. 139–147, 2019.
- [10] T. Sorensen, "A method of establishing groups of equal amplitude in plant sociology based on similarity of species and its application to analyses of the vegetation on Danish commons," *Kongelige Danske Videnskabernes Selskab*, vol. 5, no. 4, 1948.
- [11] L. R. Dice, "Measures of the amount of ecologic association between species," *Ecology*, vol. 26, no. 3, pp. 297–302, 1945.
- [12] W. GroB, "Grundzüge der Mengenlehre," *Monatshefte für Mathematik und Physik*, vol. 26, no. 1, pp. A34–A35, 1915.
- [13] PyTorch Serve Contributors, *Model Serving on Pytorch. GitHub-TorchServe*, <https://github.com/pytorch/serve>, 2021.
- [14] G. Litjens, F. Ciompi, J. M. Wolterink et al., "State-of-the-Art deep learning in cardiovascular image analysis," *Journal of the American College of Cardiology: Cardiovascular Imaging*, vol. 12, no. 8, pp. 1549–1565, 2019.
- [15] M. Sermesant, H. Delingette, H. Cochet, P. Jaïs, and N. Ayache, "Applications of artificial intelligence in cardiovascular imaging," *Nature Reviews Cardiology*, vol. 18, no. 8, pp. 600–609, 2021.
- [16] P. Morais, J. L. Vilaca, S. Queiros et al., "Semiautomatic estimation of device size for left atrial appendage occlusion in 3-D TEE images," *IEEE Transactions on Ultrasonics, Ferroelectrics, and Frequency Control*, vol. 66, no. 5, pp. 922–929, 2019.
- [17] A. M. Aguado, A. L. Olivares, C. Yagüe et al., "In silico optimization of left atrial appendage occluder implantation using interactive and modeling tools," *Frontiers in Physiology*, vol. 10, 2019.
- [18] A. M. Bavo, B. T. Wilkins, P. Garot et al., "Validation of a computational model aiming to optimize preprocedural planning in percutaneous left atrial appendage closure," *Journal of Cardiovascular Computed Tomography*, vol. 14, no. 2, pp. 149–154, 2020.

Research Article

Artificial Intelligence Enabled Fully Automated CMR Function Quantification for Optimized Risk Stratification in Patients Undergoing Transcatheter Aortic Valve Replacement

Ruben Evertz ^{1,2}, Torben Lange ^{1,2}, Sören J. Backhaus ^{1,2}, Alexander Schulz,^{1,2}
Bo Eric Beuthner,^{1,2} Rodi Topci ^{1,2}, Karl Toischer,^{1,2} Miriam Puls,^{1,2}
Johannes T. Kowallick,^{2,3} Gerd Hasenfuß,^{1,2} and Andreas Schuster ^{1,2}

¹University Medical Center Göttingen (UMG), Department of Cardiology and Pneumology, Göttingen, Germany

²German Center for Cardiovascular Research (DZHK), Partner Site Göttingen, Göttingen, Germany

³University Medical Center Göttingen (UMG), Department of Diagnostic & Interventional Radiology, Göttingen, Germany

Correspondence should be addressed to Andreas Schuster; andreas_schuster@gmx.net

Received 15 October 2021; Revised 20 December 2021; Accepted 21 March 2022; Published 20 April 2022

Academic Editor: Michael C. Kim

Copyright © 2022 Ruben Evertz et al. This is an open access article distributed under the Creative Commons Attribution License, which permits unrestricted use, distribution, and reproduction in any medium, provided the original work is properly cited.

Background. Cardiovascular magnetic resonance imaging is considered the reference standard for assessing cardiac morphology and function and has demonstrated prognostic utility in patients undergoing transcatheter aortic valve replacement (TAVR). Novel fully automated analyses may facilitate data analyses but have not yet been compared against conventional manual data acquisition in patients with severe aortic stenosis (AS). **Methods.** Fully automated and manual biventricular assessments were performed in 139 AS patients scheduled for TAVR using commercially available software (suiteHEART®, Neosoft; QMass®, Medis Medical Imaging Systems). Volumetric assessment included left ventricular (LV) mass, LV/right ventricular (RV) end-diastolic/end-systolic volume, LV/RV stroke volume, and LV/RV ejection fraction (EF). Results of fully automated and manual analyses were compared. Regression analyses and receiver operator characteristics including area under the curve (AUC) calculation for prediction of the primary study endpoint cardiovascular (CV) death were performed. **Results.** Fully automated and manual assessment of LVEF revealed similar prediction of CV mortality in univariable (manual: hazard ratio (HR) 0.970 (95% CI 0.943–0.997) $p = 0.032$; automated: HR 0.967 (95% CI 0.939–0.995) $p = 0.022$) and multivariable analyses (model 1: (including significant univariable parameters) manual: HR 0.968 (95% CI 0.938–0.999) $p = 0.043$; automated: HR 0.963 [95% CI 0.933–0.995] $p = 0.024$; model 2: (including CV risk factors) manual: HR 0.962 (95% CI 0.920–0.996) $p = 0.027$; automated: HR 0.954 (95% CI 0.920–0.989) $p = 0.011$). There were no differences in AUC (LVEF fully automated: 0.686; manual: 0.661; $p = 0.21$). Absolute values of LV volumes differed significantly between automated and manual approaches ($p < 0.001$ for all). Fully automated quantification resulted in a time saving of 10 minutes per patient. **Conclusion.** Fully automated biventricular volumetric assessments enable efficient and equal risk prediction compared to conventional manual approaches. In addition to significant time saving, this may provide the tools for optimized clinical management and stratification of patients with severe AS undergoing TAVR.

1. Introduction

Cardiovascular disease remains the leading cause of death globally. Aortic stenosis (AS) is the most common valvular heart disease and of rising prevalence in the elderly population. Transthoracic echocardiography (TTE) constitutes the standard diagnostic tool to quantify AS using

transvalvular gradients and velocities. However, in the absence of a high-gradient situation, the diagnostic work is challenging and includes accurate determination of left ventricular (LV) ejection fraction (EF) and LV stroke volume (SV) to distinguish between different AS subgroups [1]. Furthermore, cardiac function has strong prognostic implications in patients with AS and other structural heart

diseases, and therefore, its accurate determination is essential for clinical management and risk prediction [1–5]. Amongst various imaging techniques, cardiovascular magnetic resonance (CMR) imaging is considered a reference methodology with proven superiority over echocardiographical analyses regarding reproducibility and accuracy to detect clinically significant alterations in LV and right ventricular (RV) dimensions and function [6–9]. Recently, novel artificial intelligence (AI)-based deep-learning algorithms were introduced, enabling accurate and fully automated image analyses using convolutional neural networks [10–12]. These AI-based volumetric analyses were already shown to be feasible, reproducible, and of prognostic value in patients with coronary disease and were of high potential for time saving and facilitation of clinical routine [13, 14]. However, similar data in patients with severe AS are currently lacking. Therefore, we sought to investigate fully automated biventricular volumetric analyses using commercially available software solutions in comparison to conventional manual analyses and to study their accuracy in terms of volumetric assessment and prognostic implications in patients with severe AS being scheduled for transcatheter aortic valve replacement (TAVR).

2. Methods

2.1. Study Population. Patients fulfilling echocardiographic criteria of severe AS according to current guidelines of the European Society of Cardiology and confirmed indications for TAVR without typical contraindications for CMR were able to participate [1, 15, 16]. Between January 2017 and June 2021, a total of 146 patients were prospectively enrolled and agreed to an additional CMR before undergoing TAVR as part of an interdisciplinary research project on aortic valve stenosis [17]. The local ethics committee approved the study, and written informed consent was obtained from all patients. The study was conducted according to the principles of the Helsinki Declaration.

2.2. Clinical End Points. Death from cardiovascular (CV) reason according to the VARC-3 definition was defined as the clinical end point of this study [18].

2.3. CMR Analyses. CMR imaging was performed on a 3 Tesla MR scanner (MAGNETOM Skyra, Siemens Healthcare, Erlangen, Germany) using a 32-channel surface coil. The standardized scanning protocol has been reported elsewhere and included long- and short-axis (SAX) steady-state free precession images (repetition time, 3.2 ms; echo time, 1.2 ms; flip angle, 60°; slice thickness 8 mm) [19]. An experienced investigator performed manual volumetric analyses in short-axis orientation using a dedicated post-processing software (QMass®, Version 3.2.36.4, Medis Medical Imaging Systems, Leiden, Netherlands) according to current clinical recommendations including papillary muscles within the myocardium [20]. For automated volumetric analyses, commercially available AI software provided by Neosoft (suiteHEART, Version 5.0.0, Neosoft,

Pewaukee, Wisconsin, USA) was used. In a first step, after uploading the complete dataset of all patients, fully automated analyses were performed overnight without any further postprocessing user interaction. Afterwards, all automatically traced endocardial and epicardial borders were reviewed visually and adapted in case of insufficient border delineation. Furthermore, the time needed for visual border validation and, if required, contour correction was recorded. Volumetric analyses included LV mass, LV and RV end-diastolic/-systolic (EDV/ESV) volumes, stroke volume (SV), and LV and RV EF (Figure 1).

2.4. Statistical Analysis. Statistical analysis was performed using IBM SPSS Statistics version 27 for Windows (International Business Machines Corporation (IBM® Corp.), Armonk, New York, United States of America) and Microsoft Excel 2016 (Microsoft Corporation, Redmond, Washington, USA). Normal distribution for continuous data was tested using the Shapiro–Wilk test. Data were compared using the Mann–Whitney *U* or Student’s *t*-test as appropriate and expressed as median and interquartile range. Intergroup comparison of categorical variables was performed using the χ^2 test, and data were presented as absolute numbers and percentages. Dependent variables were tested using the Wilcoxon signed rank test or Student’s *t*-test for paired samples as appropriate. Assessment of the manual and automated analyses agreement was performed first by calculation of the intraclass correlation coefficients (ICC), which was scored as excellent (>0.74), good (0.6–0.74), fair (0.4–0.59), and poor (<0.4), second by Bland–Altman analysis (mean difference between measurements with 95% confidence interval (CI)), and third by the coefficient of variation (COV) [21, 22]. COV was defined as the standard deviation of the differences divided by the mean [23]. Univariable calculations were used to identify determinants of the predefined end point and included in multivariable calculations if $p < 0.05$ (model 1). In a second model, classical CV risk factors were additionally included (age, hypertension, diabetes mellitus, dyslipidaemia, and coronary heart disease). Results of regression analyses were expressed as hazard ratio (HR) with corresponding 95% confidence intervals (CIs). To assess the additional predictive value of automatically generated volumetric parameters, receiver operator characteristics (ROC) were implemented. For both manual and automatic measurements, the area under the curve (AUC) for predicting the endpoint was calculated and compared using the nonparametric approach by DeLong et al. [24].

3. Results

3.1. Study Population. While the initial study population consisted of 146 patients, the final cohort after withdrawal was 142 patients. These consisted of 71 patients (50.0%) with normal ejection fraction high gradient (NEFHG) AS; 19 patients (13.4%) with low ejection fraction high gradient (LEFHG) AS; 21 patients (14.8%) with low ejection fraction low gradient (LEFLG) AS; and 31 patients (21.8%) with

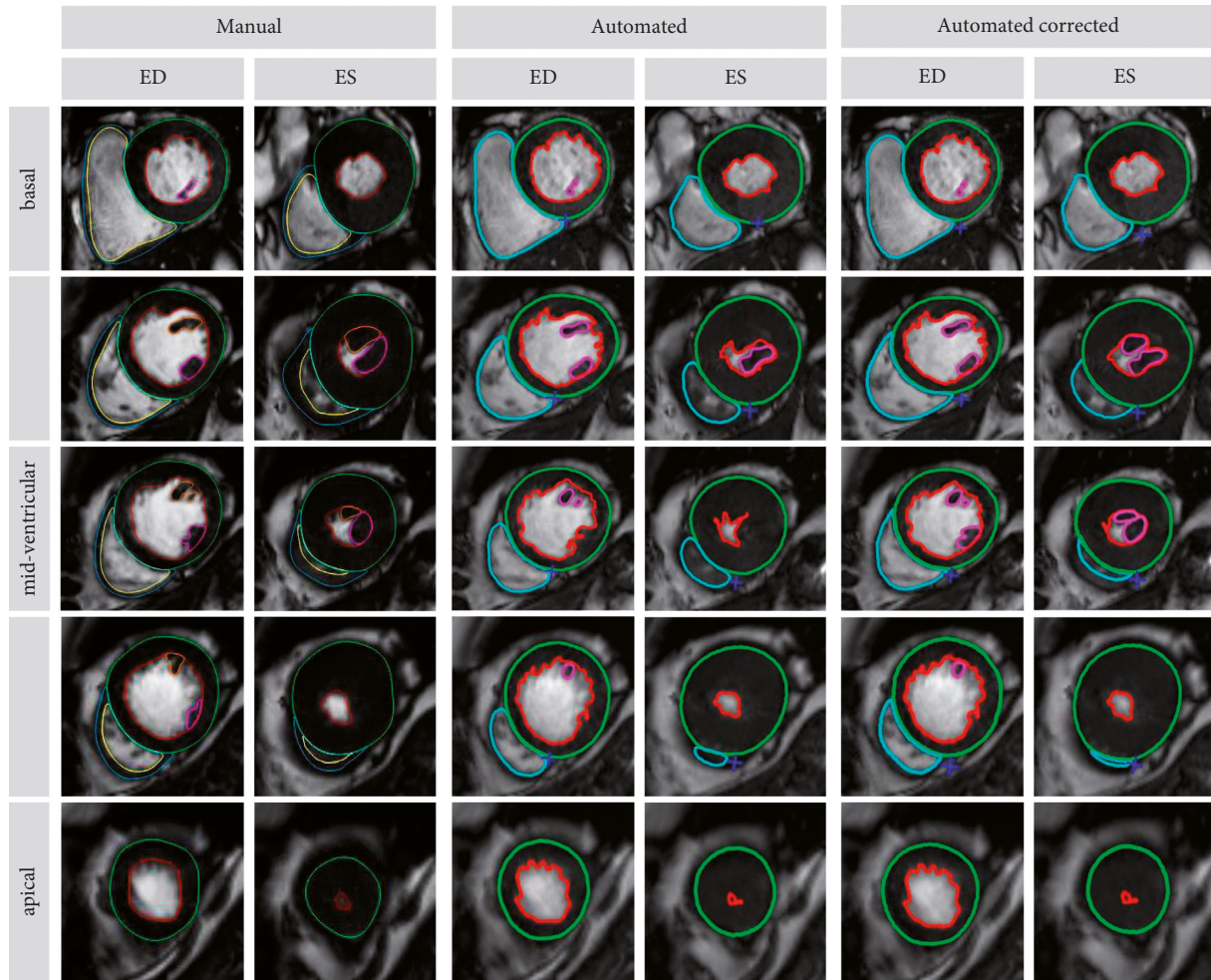


FIGURE 1: Manual, automated, and automated-corrected biventricular volumetric analyses. Overview of a tracked short-axis stack from the base to apex in end-diastole (ED) and end-systole (ES) using manual and automated analysis software.

paradoxical low flow low gradient (PLFLG) AS. Mean age of the study population was 78 ± 6 years with age ranging from 59 to 90 years. The majority of patients (62%, $n = 88$) were male. Predominant comorbidities were hypertension (85.9%) followed by coronary artery disease (65.5%), atrial fibrillation (32.4%), stroke/transient ischemic attack (TIA) (12.7%), and chronic obstructive pulmonary disease (COPD) (9.9%). CV death occurred in 12.0% of patients. There were no differences between survivors and deceased patients in regard to age, sex, and comorbidities. However, deceased patients' BMI was slightly higher compared to survivors ($p = 0.017$). Details are displayed in Table 1.

3.2. Automated and Manual Assessment of the Volumetric Parameters. Of the finally included 142 patients, 142 (100%) patients were analyzed manually and 139 (97.9%) patients automatically, because the fully automated analysis did not work. Therefore, further analyses were performed with the remaining 139 patients.

Differences between manual and automated biventricular segmentation are presented in Table 2. LV mass was estimated higher and LV volumes lower using

automated analyses compared to manual analyses (LV mass index (g/m^2) automated vs. manual: $88.0 [75.0-111.0]$ vs. $83.3 [69.4-102.8]$; LVEDV index (ml/m^2) automated vs. manual: $71.3 [60.0-88.8]$ vs. $78.3 [63.3-97.3]$; LVESV index (ml/m^2) automated vs. manual: $27.7 [16.0-45.6]$ vs. $31.1 [17.9-44.9]$ all $p < 0.001$). The opposite was true for RV volumes with statistically significant differences for RVEDV (RVEDV index (ml/m^2) automated vs. manual: $69.4 [58.4-83.0]$ vs. $67.3 [56.9-80.8]$ $p < 0.001$; RVESV index (ml/m^2) automated vs. manual: $31.7 [22.7-39.9]$ vs. $31.4 [23.1-44.4]$ $p = 0.07$). RVEF was higher using automated analyses, but not LVEF (RVEF (%) automated vs. manual: $55.0 [9.0-61.0]$ vs. $53.6 [44.2-59.7]$ $p = 0.01$; LVEF (%) automated vs. manual: $62.0 [46.0-73.0]$ vs. $60.3 [45.9-73.4]$ $p = 0.889$). Similar findings were observed in AS subgroups and are presented in the online data supplement (Tables S1–S4).

Table 3 illustrates the agreement of fully automated and manual analyses including bias with 95% limits of agreement (LOA), ICC, and COV. In addition, Bland–Altman plots are presented in Figure 2. Overall, for both the LV and RV measurements, high agreement was found between manual and automated analyses. However, LV parameters showed

TABLE 1: Baseline characteristics

Variable	All patients (n = 142)	Survivors (n = 125)	CV deceased (n = 17)	p value
Age (Y)	80 (74–83)	79 (74–82)	82 (78.5–84)	0.069
Sex (male)	88 (62.0%)	77 (61.6%)	11 (64.7%)	0.805
BMI (kg/m ²)	27.5 (24.6–30.7)	27.0 (24.4–30.2)	30.8 (26.9–33.5)	0.014
Comorbidities				
Hypertension	122 (85.9%)	107 (85.6%)	15 (88.2%)	1.000
Diabetes mellitus	46 (32.4%)	37 (29.6%)	9 (52.9%)	0.054
Dyslipidaemia	97 (68.3%)	86 (68.8%)	11 (64.7%)	0.866
Coronary artery disease	93 (65.5%)	80 (64.0%)	13 (76.5%)	0.310
Atrial fibrillation	46 (32.4%)	38 (30.4%)	8 (47.1%)	0.168
Stroke/TIA	18 (12.7%)	16 (12.8%)	2 (11.8%)	0.926
COPD	14 (9.9%)	10 (8.0%)	4 (23.5%)	0.066

Data are expressed as median (interquartile range), numbers, and percentage. Comparison of survivors and deceased was performed. Continuous parameters were tested for normal distribution using the Shapiro–Wilk test and compared using the Mann–Whitney *U* test or *t*-test as appropriate. Categorical parameters were tested using the chi-square test. BMI: body mass index; TIA: transient ischemic attack; COPD: chronic obstructive pulmonary disease.

TABLE 2: Biventricular volumes based on CMR measurements.

Left ventricle	Automated (uncorrected)	Manual	p value
LV mass (g)	170.1 (139.1–213.9)	161 (132.0–199.2)	<0.001
LV mass index (g/m ²)	88.0 (75.0–111.0)	83.3 (69.4–102.8)	<0.001
LV EDV index (ml/m ²)	71.3 (60.0–88.8)	78.3 (63.3–97.3)	<0.001
LV ESV index (ml/m ²)	27.7 (16.0–45.6)	31.1 (17.9–44.9)	<0.001
LV SV index (ml/m ²)	42.8 (35.3–49.3)	45.5 (36.7–53.9)	<0.001
LVEF (%)	62.0 (46.0–73.0)	60.3 (45.9–73.4)	0.889
Right ventricle	Automated (uncorrected)	Manual	p value
RV EDV index (ml/m ²)	69.4 (58.4–83.0)	67.3 (56.9–80.8)	<0.001
RV ESV index (ml/m ²)	31.7 (22.7–39.9)	31.4 (23.1–44.4)	0.07
RV SV index (ml/m ²)	38.6 (31.4–45.0)	35.2 (28.8–43.4)	<0.001
RVEF (%)	55.0 (49.0–61.0)	53.6 (44.2–59.7)	0.01

Continuous data were compared using the Wilcoxon signed rank test and are expressed as median (interquartile range). EDV: end-diastolic volume; ESV: end-systolic volume; LV: left ventricular; LVEF: left ventricular ejection fraction; RV: right ventricular; RVEF: right ventricular ejection fraction; SV: stroke volume.

TABLE 3: Agreement between manual and automated uncorrected analyses.

Left ventricle	Bias	95% LOA	ICC (95% CI)	COV (%)
LV mass (g)	–10.08	–84.2 to 64.1	0.890 (0.846–0.921)	21.5
LV EDV (ml)	11.13	–23.5 to 45.8	0.978 (0.969–0.984)	11.2
LV ESV (ml)	4.63	–22.6 to 31.9	0.983 (0.977–0.988)	19.5
LV SV (ml)	6.69	–17.6 to 31.0	0.935 (0.909–0.954)	14.4
LVEF (%)	0	–12.1 to 12.1	0.964 (0.950–0.975)	10.5
Right ventricle	Bias	95% LOA	ICC (95% IC)	COV (%)
RV EDV (ml)	–3.44	–40.7 to 33.8	0.954 (0.936–0.967)	13.6
RV ESV (ml)	1.37	–26.6 to 29.4	0.955 (0.938–0.968)	21.0
RV SV (ml)	–4.26	–37.1 to 28.6	0.832 (0.765–0.880)	23.3
RVEF (%)	–2.44	–21.7 to 16.9	0.804 (0.725–0.860)	18.6

EDV: end-diastolic volume; ESV: end-systolic volume; LV: left ventricular; LVEF: left ventricular ejection fraction; RV: right ventricular; RVEF: right ventricular ejection fraction; SV: stroke volume.

better agreement than RV parameters for LVEF (bias: 0; 95% LOA: –12.1 to 12.1; ICC 0.964; COV: 10.5), LVEDV (bias: 11.13; 95% LOA: –23.5 to 45.8; ICC 0.978; COV: 11.2), and LVESV (bias 4.63; 95% LOA: –22.6 to 31.9; ICC 0.983; COV: 19.5) as compared to RVEF (bias: –2.44; 95% LOA: –21.7 to 16.9; ICC 0.804; COV: 18.6), RVEDV (bias: –3.44; 95% LOA: –40.7 to 33.8; ICC 0.954; COV: 13.6), and RVESV (bias: 1.37; 95% LOA: –26.6 to 29.4; ICC 0.955; COV: 21.0). Data for

corresponding subgroup analyses are presented in the online data supplement (Tables S5–S8).

Manual postprocessing volumetric analyses took on average 13 minutes by an experienced operator. In contrast, using fully automated software took on average 45 seconds for volumetric analyses. The consequent operator review of the correct contour detection took 60 seconds on average. Correction of the contours took another 60 seconds on

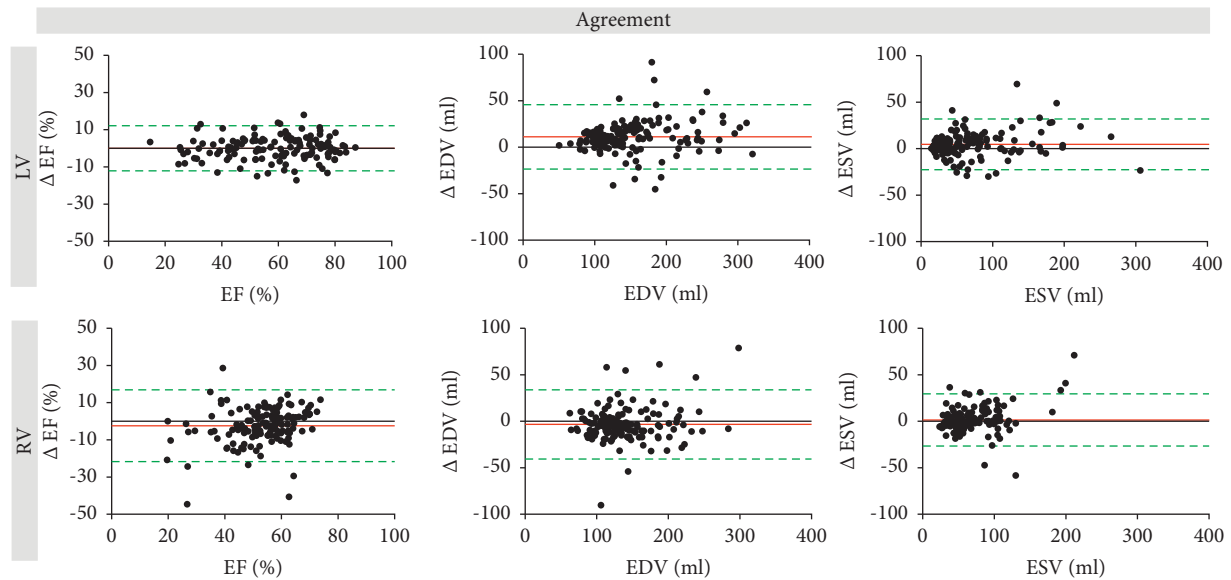


FIGURE 2: Bland–Altman plots for agreement of manual and automated biventricular volumes. LV: left ventricular; RV: right ventricular; EF: ejection fraction; EDV: end-diastolic volume; ESV: end-systolic volume.

TABLE 4: Agreement between manual and automated corrected analyses.

Left ventricle	Bias	95% LOA	ICC (95% CI)	COV (%)
LV mass (g)	−9.91	−83.6 to 63.8	0.891 (0.848–0.922)	21.4
LV EDV (ml)	11.47	−22.5 to 45.4	0.979 (0.971–0.985)	11.0
LV ESV (ml)	4.77	−20.8 to 30.3	0.985 (0.979–0.989)	18.4
LV SV (ml)	6.89	−15.8 to 29.6	0.944 (0.921–0.960)	13.5
LVEF (%)	0.03	−10.2 to 10.2	0.975 (0.965–0.982)	8.8
Right ventricle	Bias	95% LOA	ICC (95% IC)	COV (%)
RV EDV (ml)	−3.48	−40.7 to 33.7	0.954 (0.936–0.967)	13.6
RV ESV (ml)	1.44	−25.5 to 28.4	0.958 (0.942–0.970)	20.3
RV SV (ml)	−4.35	−36.3 to 27.6	0.841 (0.778–0.886)	22.7
RVEF (%)	−2.47	−21.4 to 16.5	0.810 (0.735–0.864)	18.3

EDV: end-diastolic volume; ESV: end-systolic volume; LV: left ventricular; LVEF: left ventricular ejection fraction; RV: right ventricular; RVEF: right ventricular ejection fraction; SV: stroke volume.

average if needed. In 22 patients (15.8%), minor manual corrections of the myocardial borders mainly in the most basal or apical slices were performed resulting in a better agreement with manual analyses (Table 4).

3.3. Prognostic Value of Automated and Manual Assessments.

The mean follow-up period was 760 ± 439 days. During this period a total of 27 patients (19.4%) died, whereas in 17 cases (12.2%), a cardiovascular death occurred. Cox regression univariable modelling revealed that BMI (HR 1.090 (95% CI 1.001–1.187) $p = 0.048$) and the presence of COPD (HR 3.090 (95% CI 1.005–9.501) $p = 0.048$) were associated with increased CV mortality. Regarding volumetric parameters, both manual and automated LVEF were associated with the occurrence of CV death (manual: HR 0.970 (95% CI 0.943–0.997) $p = 0.032$; automated: HR 0.967 (95% CI 0.939–0.995) $p = 0.022$). LVEF, derived manually or fully automatically, remained a significant predictor of CV death on multivariable modelling including significant univariable parameters (manual: HR 0.968 (95% CI 0.938–0.999)

$p = 0.043$; automated: HR 0.963 (95% CI 0.933–0.995) $p = 0.024$]. In a second model, classical CV risk factors were additionally included (age, hypertension, diabetes mellitus, dyslipidaemia, coronary heart disease). LVEF remained a significant predictor of CV death (manual: HR 0.962 (95% CI 0.920–0.996) $p = 0.027$; automated: HR 0.954 (95% CI 0.920–0.989) $p = 0.011$). In either model, BMI was also an independently significant risk predictor. A detailed overview is given in Table 5.

There were no significant differences seen between fully automated, automated corrected, and manual LVEFs on AUC comparison (fully automated: AUC 0.686; automated corrected: AUC: 0.671; manual: AUC 0.661; fully automated vs. automated corrected: $p = 0.115$, fully automated vs. manual: $p = 0.214$, automated corrected vs. manual: $p = 0.545$).

4. Discussion

To our knowledge, this is the first study investigating the applicability of an AI-based fully automated biventricular volumetric and functional analysis with demonstrated

TABLE 5: Univariable and multivariable cox regression analyses including LVEF for prediction of CV mortality.

Variable	Hazard ratio (95% CI)	<i>p</i> value
Univariable models		
Age (Y)	1.074 (0.978–1.178)	0.135
Sex (male)	1.195 (0.438–3.261)	0.727
BMI (kg/m ²)	1.090 (1.001–1.187)	0.048
Hypertension (present)	1.054 (0.240–4.623)	0.944
Diabetes mellitus (present)	2.196 (0.846–5.700)	0.106
Dyslipidaemia (present)	0.953 (0.347–2.618)	0.925
Coronary artery disease (present)	1.888 (0.614–5.811)	0.268
Atrial fibrillation (present)	2.372 (0.907–6.198)	0.078
Stroke/TIA (present)	0.816 (0.186–3.573)	0.787
COPD (present)	3.090 (1.005–9.501)	0.049
Automated LVEF (%)	0.967 (0.939–0.995)	0.022
LVEF (%)	0.970 (0.943–0.997)	0.032
Automated LV SVI (ml/m ²)	0.996 (0.952–1.042)	0.859
LV SVI (ml/m ²)	0.999 (0.961–1.039)	0.965
Multivariable models		
Model 1a		
Automated LVEF (%)	0.963 (0.933–0.995)	0.024
BMI (kg/m ²)	1.130 (1.029–1.241)	0.011
COPD (present)	2.277 (0.691–7.507)	0.451
Model 1b		
LVEF (%)	0.968 (0.938–0.999)	0.043
BMI (kg/m ²)	1.126 (1.025–1.237)	0.013
COPD (present)	2.400 (0.718–8.014)	0.155
Model 2a		
Automated LVEF (%)	0.954 (0.920–0.989)	0.011
BMI (kg/m ²)	1.162 (1.024–1.320)	0.020
COPD (present)	1.718 (0.414–7.123)	0.456
Age (Y)	2.231 (0.742–6.704)	0.153
Diabetes mellitus (present)	2.231 (0.742–6.704)	0.153
Hypertension (present)	2.128 (0.397–11.417)	0.378
Dyslipidaemia (present)	0.662 (0.209–2.090)	0.482
Coronary artery disease (present)	1.363 (0.391–4.747)	0.627
Model 2b		
LVEF (%)	0.962 (0.929–0.996)	0.027
BMI (kg/m ²)	1.139 (1.014–1.280)	0.028
COPD (present)	2.000 (0.494–8.102)	0.331
Age (Y)	1.113 (0.345–4.406)	0.055
Diabetes mellitus (present)	2.385 (0.798–7.121)	0.120
Hypertension (present)	1.846 (0.356–9.578)	0.465
Dyslipidaemia (present)	0.655 (0.209–2.055)	0.468
Coronary artery disease (present)	1.233 (0.345–4.406)	0.747

BMI: body mass Index; TIA: transient ischemic attack; COPD: chronic obstructive pulmonary disease; LVEF: left ventricular ejection fraction; LV SVI: left ventricular stroke volume index

clinical utility and predictive value for optimized risk stratification in patients with severe AS. The following findings are notable: Firstly, fully automatically derived CMR-based LVEF has a similar significant association with mortality compared to conventional analyses with the advantage of a substantial time saving. Secondly, automatically calculated results seem sufficient for risk prediction without a mandatory user interaction by a CMR imaging specialist. Thirdly, AI-based CMR postprocessing software facilitates

the use and widens the applicability of CMR imaging with potential fast and easy integration into clinical routine.

The rising incidence of valvular heart diseases is inevitably associated with an increased need for economical and accurate diagnostic procedures. Especially CMR imaging plays a key role amongst noninvasive imaging techniques due to its comprehensive myocardial analysis tools. However, its postprocessing routine is still laborious and time consuming [8]. Recently, automated postprocessing software solutions based on deep-learning algorithms have been developed and are already commercially available with proven clinical utility [11, 25, 26].

AI software has been already applied in various cardiovascular diseases and shown to offer similar or even improved risk stratification compared to manual approaches [27]. Applications are wide ranging and demonstrate that a patient-centred individual approach, for example, using machine learning multiprotein risk models, allows a better detection of future events than currently used clinical risk scores [28]. Recently, the field of applications has also been extended to optimized screening and diagnosis procedures including subtle ECG alterations in patients with AS [29, 30]. Amongst the parameters for clinical decision making, especially the LVEF has a pivotal role for optimized patient management with important prognostic implications that were proven in various different studies comprising common CV diseases like acute myocardial infarction or heart failure [2, 31, 32]. Furthermore, clinical decisions like the indication for the implantation of an implantable cardioverter defibrillator are based on the LVEF [2]. In addition, in patients with severe AS scheduled for aortic valve replacement, data have shown an important association between mortality and LVEF [33, 34]. In line with these findings, our results showed significant associations of the LVEF with CV mortality independently of whether a fully automated or conventional analysis approach was used. Therefore, applying fully automated volumetric analyses in patients with severe AS is feasible and offers an attractive alternative postprocessing approach compared to manual segmentation with equal prognostic implications. Although the LVEF might not be the one complete parameter to describe the prognosis of all AS patients, for example, aortic valve calcification or global longitudinal strain measurements might be the more important parameters for optimized prognosis evaluation in different subgroups of AS, the LVEF and the SV have important roles to define respective AS subgroups and, therefore, their accurate assessment has a crucial role in clinical routine [35, 36]. Furthermore, our results are similar to the predictive value of LVEF in a large cohort of patients with acute myocardial infarction and therefore confirm a certain predictive value of this parameter in patients with AS [13].

Besides an equal risk prediction, there were numerical differences between fully automatically assessed volumetric parameters compared to manual segmentation by an experienced CMR operator in our study. Fully automated measurements resulted in larger LV mass and smaller LV volumes; however, the LVEF showed no statistically significant difference. These results are contrary to previous studies applying AI-based fully automated quantification that documented smaller LV mass but larger volumes [13, 14]. These differences

might be caused by a slightly different volumetric approach excluding the papillary muscles and trabecular endocardial tissue in the aforementioned studies. Since an exact delineation of trabecular tissue using manual analysis software is tedious and partially limited due to automated smoothing of the analysis software, the automated approach might provide a more exact representation of myocardial volumetric relations. Nevertheless, in line with the aforementioned studies, the documented agreement of volumetric parameters was excellent in our study with LVEF having the lowest bias. In terms of biventricular agreement, LV measurements were better than RV segmentations, which might be explainable by the more complex anatomy of the RV which has also been described in previous CMR studies [14, 37].

Even though fully automated analysis was successful in the majority of the study population (97.9%), a visual review of the automated contours and their adaptation, if necessary, by the CMR operator was performed in our study and resulted in an improved agreement of volumetric parameters. However, the corrections did not enable an improved risk stratification, and therefore, a direct clinical use of the parameters without a categorically needed review of the delineations could be envisaged. Although one might consider to omit visual review of the contours as a consequence, individual level CIs of -12.1 to 12.1 for LVEF and even wider ranges for LV volumes underline the importance of a visual review and corrections in case of insufficient border delineation. As previously described, a relevant proportion of patients required manual border adjustments especially in basal and apical slices which are the most challenging areas of myocardial volumetric analyses bringing current automated software solutions to their delineation limits [13, 38].

However, the decisive advantage of AI-based software in the field of CMR postprocessing is a remarkable saving of time, which is underlined by the results of our study. Compared to manual analysis, the AI-based software provided about 10 saved minutes for volumetric assessments on a per-patient basis. The time saving use of fully automated software can be even increased by using it “on-the-fly” during imaging acquisition or overnight. This does not only result in a more efficient postprocessing practice during clinical routine but also in facilitated analyses of large patient cohorts and, consequently, might even be accompanied by lower costs of CMR imaging procedures.

In addition to the time-saving aspect, AI solutions offer more user-independent measurements and can improve comparability of parameters in serial examinations or between CMR core laboratories of different hospitals. The excellent intra-observer and interobserver reproducibility for fully automated volumetric assessment that exceeds the reproducibility of manual assessments has been described previously by Backhaus et al. [14]. With a more widespread availability of MRI scanners and increasing incidences of patients with AS and consequently rising numbers of interventional valve replacement procedures, AI-based software therefore constitutes a key tool for accurate and efficient volumetric assessment in clinical routine even for nonimaging specialists.

4.1. Study Limitations. Some limitations need to be addressed. Firstly, due to typical CMR contraindications only selected patients were able to participate in this study. Secondly, only patients considered stable and being able to lie in a supine position were included. Both contraindications and the ability to undergo CMR scanning might have led to a selection bias and resulting in lower event rates by excluding potentially sicker patients. However, these limitations apply to both analysis techniques and therefore do not limit the validity of the analysis. Thirdly, detailed information of the AI-based algorithm is not disclosed by the manufacturer and therefore cannot be described in more detail. Thirdly, the fully automated software does not offer RV mass quantification yet, and consequently, this parameter was not analyzed in our study. Fourthly, a total of three patients (2.1%) could not be analyzed using the automated algorithm, which needs to be considered especially when studying dyspneic patients such as AS patients. Finally, we have observed small numerical differences between fully automated and manual volumetric assessments. Consequently, on an individual patient level final contours and results should always be approved or corrected by a responsible physician to also allow comparability between repeated scans, e.g., before and after TAVR.

5. Conclusion

Fully automated assessment of biventricular volumes and function is feasible and enables similar risk prediction compared to a conventional manual approach in patients with severe aortic stenosis scheduled for TAVR. Agreement between manual and fully automated analyses is excellent, and manual correction of border delineation does not lead to an improved risk prediction. Due to its accuracy and immense time-saving nature, application of AI software enables a more widespread user-independent risk stratification and may facilitate easy implementation of CMR imaging in clinical routine prior to TAVR. Further studies are needed to validate these findings to fully establish this technique in clinical routine.

Data Availability

Regarding data availability, we confirm that all relevant data are included within the paper and all data underlying the findings are fully available without restriction and can be accessed at the University Medical Centre Goettingen by researchers who meet the criteria for access to confidential data.

Ethical Approval

This study was conducted according to the guidelines of the Declaration of Helsinki and approved by the local ethics committee of the University Medical Center Göttingen (10/5/16).

Consent

Informed consent was obtained from all subjects involved in the study.

Disclosure

This research was performed as part of the employment of the authors (University Medical Center Göttingen, Department of Cardiology and Pneumology).

Conflicts of Interest

The authors declare that there are no conflicts of interest regarding the publication of this article.

Authors' Contributions

Ruben Evertz and Torben Lange contributed equally to this work.

Supplementary Materials

Table S1: biventricular volumes based on CMR measurements in patients with normal ejection fraction high gradient aortic stenosis ($n = 68$). Table S2: biventricular volumes based on CMR measurements in patients with low ejection fraction high gradient aortic stenosis ($n = 19$). Table S3: biventricular volumes based on CMR measurements in patients with low ejection fraction low gradient aortic stenosis ($n = 21$). Table S4: biventricular volumes based on CMR measurements in patients with paradoxical low flow low gradient aortic stenosis ($n = 31$). Table S5: agreement between manual and automated uncorrected analyses in patients with normal ejection fraction high gradient aortic stenosis ($n = 68$). Table S6: agreement between manual and automated uncorrected analyses in patients with low ejection fraction high gradient aortic stenosis ($n = 19$). Table S7: agreement between manual and automated uncorrected analyses in patients with low ejection fraction low gradient aortic stenosis ($n = 21$). Table S8: agreement between manual and automated uncorrected analyses in in patients with paradoxical low flow low gradient aortic stenosis ($n = 31$). (*Supplementary Materials*)

References

- [1] A. Vahanian, F. Beyersdorf, F. Praz et al., “2021 ESC/EACTS guidelines for the management of valvular heart disease,” *European Heart Journal*, vol. 43, no. 7, pp. 561–632, 2021.
- [2] T. A. McDonagh, M. Metra, M. Adamo et al., “2021 ESC Guidelines for the diagnosis and treatment of acute and chronic heart failure,” *European Heart Journal*, vol. 42, 2021.
- [3] Y. Bohbot, C. de Meester de Ravenstein, G. Chadha et al., “Relationship between left ventricular ejection fraction and mortality in asymptomatic and minimally symptomatic patients with severe aortic stenosis,” *Journal of the American College of Cardiology: Cardiovascular Imaging*, vol. 12, no. 1, pp. 38–48, 2019.
- [4] J. Knuuti, W. Wijns, A. Saraste et al., “2019 ESC Guidelines for the diagnosis and management of chronic coronary syndromes,” *European Heart Journal*, vol. 41, pp. 407–477, 2020.
- [5] S. Ito, W. R. Miranda, V. T. Nkomo et al., “Reduced left ventricular ejection fraction in patients with aortic stenosis,” *Journal of the American College of Cardiology*, vol. 71, no. 12, pp. 1313–1321, 2018.
- [6] F. Grothues, J. C. Moon, N. G. Bellenger, G. S. Smith, H. U. Klein, and D. J. Pennell, “Interstudy reproducibility of right ventricular volumes, function, and mass with cardiovascular magnetic resonance,” *American Heart Journal*, vol. 147, no. 2, pp. 218–223, 2004.
- [7] F. Grothues, G. C. Smith, J. C. C. Moon et al., “Comparison of interstudy reproducibility of cardiovascular magnetic resonance with two-dimensional echocardiography in normal subjects and in patients with heart failure or left ventricular hypertrophy,” *The American Journal of Cardiology*, vol. 90, no. 1, pp. 29–34, 2002.
- [8] D. J. Pennell, “Cardiovascular magnetic resonance,” *Circulation*, vol. 121, no. 5, pp. 692–705, 2010.
- [9] C. A. Miller, K. Pearce, P. Jordan et al., “Comparison of real-time three-dimensional echocardiography with cardiovascular magnetic resonance for left ventricular volumetric assessment in unselected patients,” *European Heart Journal—Cardiovascular Imaging*, vol. 13, no. 2, pp. 187–195, 2012.
- [10] W. Bai, M. Sinclair, G. Tarroni et al., “Automated cardiovascular magnetic resonance image analysis with fully convolutional networks,” *Journal of Cardiovascular Magnetic Resonance*, vol. 20, no. 1, p. 65, 2018.
- [11] O. Bernard, A. Lalande, C. Zotti et al., “Deep learning techniques for automatic MRI cardiac multi-structures segmentation and diagnosis: is the problem solved?” *IEEE Transactions on Medical Imaging*, vol. 37, no. 11, pp. 2514–2525, 2018.
- [12] S. J. Backhaus, A. Schuster, T. Lange et al., “Impact of fully automated assessment on interstudy reproducibility of biventricular volumes and function in cardiac magnetic resonance imaging,” *Scientific Reports*, vol. 11, no. 1, Article ID 11648, 2021.
- [13] A. Schuster, T. Lange, S. J. Backhaus et al., “Fully automated cardiac assessment for diagnostic and prognostic stratification following myocardial infarction,” *Journal of American Heart Association*, vol. 9, no. 18, Article ID e016612, 2020.
- [14] S. J. Backhaus, W. Staab, M. Steinmetz et al., “Fully automated quantification of biventricular volumes and function in cardiovascular magnetic resonance: applicability to clinical routine settings,” *Journal of Cardiovascular Magnetic Resonance*, vol. 21, no. 1, p. 24, 2019.
- [15] T. Dill, “Contraindications to magnetic resonance imaging,” *Heart*, vol. 94, no. 7, pp. 943–948, 2008.
- [16] H. Baumgartner, V. Falk, J. J. Bax et al., “2017 ESC/EACTS Guidelines for the management of valvular heart disease,” *European Heart Journal*, vol. 38, pp. 2739–2791, 2017.
- [17] B. E. C. Beuthner, R. Topci, M. Derks et al., “Interdisciplinary research on aortic valve stenosis: a longitudinal collection of biospecimens and clinical data of patients undergoing transcatheter aortic valve replacement,” *Open Journal of Bioresources*, vol. 7, 2020.
- [18] Varc-3 Writing Committee, P. Généreux, N. Piazza et al., “Valve academic research consortium 3: updated endpoint definitions for aortic valve clinical research,” *Journal of the American College of Cardiology*, vol. 77, no. 21, pp. 2717–2746, 2021.
- [19] S. J. Backhaus, T. Lange, B. E. Beuthner et al., “Real-time cardiovascular magnetic resonance T1 and extracellular volume fraction mapping for tissue characterisation in aortic stenosis,” *Journal of Cardiovascular Magnetic Resonance*, vol. 22, no. 1, p. 46, 2020.
- [20] J. Schulz-Menger, D. A. Bluemke, J. Bremerich et al., “Standardized image interpretation and post-processing in

- cardiovascular magnetic resonance—2020 update,” *Journal of Cardiovascular Magnetic Resonance*, vol. 22, no. 1, p. 19, 2020.
- [21] J. Martin Bland and D. Altman, “Statistical methods for assessing agreement between two methods of clinical measurement,” *The Lancet*, vol. 327, no. 8476, pp. 307–310, 1986.
- [22] K. Oppo, E. Leen, W. J. Angerson, T. G. Cooke, and C. S. McArdle, “Doppler perfusion index: an interobserver and intraobserver reproducibility study,” *Radiology*, vol. 208, no. 2, pp. 453–457, 1998.
- [23] G. Morton, R. Jogiya, S. Plein, A. Schuster, A. Chiribiri, and E. Nagel, “Quantitative cardiovascular magnetic resonance perfusion imaging: inter-study reproducibility,” *European Heart Journal—Cardiovascular Imaging*, vol. 13, no. 11, pp. 954–960, 2012.
- [24] E. R. DeLong, D. M. DeLong, and D. L. Clarke-Pearson, “Comparing the areas under two or more correlated receiver operating characteristic curves: a nonparametric approach,” *Biometrics*, vol. 44, no. 3, pp. 837–845, 1988.
- [25] R. Shahzad, Q. Tao, O. Dzyubachyk, M. Staring, B. P. F. Lelieveldt, and R. J. van der Geest, “Fully-automatic left ventricular segmentation from long-axis cardiac cine MR scans,” *Medical Image Analysis*, vol. 39, pp. 44–55, 2017.
- [26] M. R. Avendi, A. Kheradvar, and H. Jafarkhani, “A combined deep-learning and deformable-model approach to fully automatic segmentation of the left ventricle in cardiac MRI,” *Medical Image Analysis*, vol. 30, pp. 108–119, 2016.
- [27] J. Betancur, F. Commanneur, M. Motlagh et al., “Deep learning for prediction of obstructive disease from fast myocardial perfusion SPECT,” *Journal of the American College of Cardiology: Cardiovascular Imaging*, vol. 11, no. 11, pp. 1654–1663, 2018.
- [28] M. Unterhuber, K.-P. Kresoja, K.-P. Rommel et al., “Proteomics-enabled deep learning machine algorithms can enhance prediction of mortality,” *Journal of the American College of Cardiology*, vol. 78, no. 16, pp. 1621–1631, 2021.
- [29] D. Playford, E. Bordin, R. Mohamad, S. Stewart, and G. Strange, “Enhanced diagnosis of severe aortic stenosis using artificial intelligence: a proof-of-concept study of 530,871 echocardiograms,” *Journal of the American College of Cardiology: Cardiovascular Imaging*, vol. 13, no. 4, pp. 1087–1090, 2020.
- [30] M. Cohen-Shelly, Z. I. Attia, P. A. Friedman et al., “Electrocardiogram screening for aortic valve stenosis using artificial intelligence,” *European Heart Journal*, vol. 42, pp. 2885–2896, 2021.
- [31] B. Ibanez, S. James, S. Agewall et al., “2017 ESC guidelines for the management of acute myocardial infarction in patients presenting with ST-segment elevation: the task force for the management of acute myocardial infarction in patients presenting with ST-segment elevation of the European society of cardiology (ESC),” *European Heart Journal*, vol. 39, pp. 119–177, 2018.
- [32] S. D. Solomon, N. Anavekar, H. Skali et al., “Influence of ejection fraction on cardiovascular outcomes in a broad spectrum of heart failure patients,” *Circulation*, vol. 112, no. 24, pp. 3738–3744, 2005.
- [33] T. Taniguchi, T. Morimoto, H. Shiomi et al., “Prognostic impact of left ventricular ejection fraction in patients with severe aortic stenosis,” *JACC: Cardiovascular Interventions*, vol. 11, pp. 145–157, 2018.
- [34] J. S. Dahl, M. F. Eleid, H. I. Michelena et al., “Effect of left ventricular ejection fraction on postoperative outcome in patients with severe aortic stenosis undergoing aortic valve replacement,” *Circulation: Cardiovascular Imaging*, vol. 8, no. 4, 2015.
- [35] S. Ludwig, A. Gossling, L. Waldschmidt et al., “TAVR for low-flow, low-gradient aortic stenosis: prognostic impact of aortic valve calcification,” *American Heart Journal*, vol. 225, pp. 138–148, 2020.
- [36] B. Cosyns and M. A. Vannan, “Global longitudinal strain in severe aortic stenosis,” *European Heart Journal—Cardiovascular Imaging*, vol. 21, no. 11, pp. 1259–1261, 2020.
- [37] L. E. Hudsmith, S. E. Petersen, J. M. Francis, M. D. Robson, and S. Neubauer, “Normal human left and right ventricular and left atrial dimensions using steady state free precession magnetic resonance imaging,” *Journal of Cardiovascular Magnetic Resonance*, vol. 7, no. 5, pp. 775–782, 2005.
- [38] B. Böttcher, E. Beller, A. Busse et al., “Fully automated quantification of left ventricular volumes and function in cardiac MRI: clinical evaluation of a deep learning-based algorithm,” *International Journal of Cardiovascular Imaging*, vol. 36, no. 11, pp. 2239–2247, 2020.

Research Article

Joint Analysis of Morphological Parameters and In Silico Haemodynamics of the Left Atrial Appendage for Thrombogenic Risk Assessment

Maria Isabel Pons,¹ Jordi Mill ,¹ Alvaro Fernandez-Quilez ,^{2,3} Andy L. Olivares ,¹ Etelvino Silva,^{4,5} Tom de Potter,⁶ and Oscar Camara ¹

¹Department of Information and Communication Technologies, Pompeu Fabra University, Barcelona 08018, Spain

²Department of Radiology, Stavanger Medical Imaging Laboratory, Stavanger University Hospital, Stavanger 4036, Norway

³Department of Quality and Health Technology, Faculty of Health Sciences, University of Stavanger, Stavanger 4036, Norway

⁴Institute of Research and Innovation in Biomedical Sciences of the Province of Cadiz (INiBICA), Cadiz 11009, Spain

⁵Department of Cardiology, Puerta Del Mar University Hospital, Cadiz 11009, Spain

⁶Department of Cardiology, Cardiovascular Centre, Aalst 9300, Belgium

Correspondence should be addressed to Oscar Camara; oscar.camara@upf.edu

Received 14 October 2021; Accepted 18 February 2022; Published 14 March 2022

Academic Editor: Verena Veulemans

Copyright © 2022 Maria Isabel Pons et al. This is an open access article distributed under the Creative Commons Attribution License, which permits unrestricted use, distribution, and reproduction in any medium, provided the original work is properly cited.

Background. Atrial fibrillation (AF) is considered the most common human arrhythmia. In nonvalvular AF, around 99% of thrombi are formed in the left atrial appendage (LAA). Nevertheless, there is not a consensus in the community about the relevant factors to stratify the AF population according to thrombogenic risk. **Objective.** To demonstrate the need for combining left atrial morphological and haemodynamics indices to improve the thrombogenic risk assessment in nonvalvular AF patients. **Methods.** A cohort of 71 nonvalvular AF patients was analysed. Statistical analysis, regression models, and random forests were used to analyse the differences between morphological and haemodynamics parameters, extracted from computational simulations built on 3D rotational angiography images, between patients with and without transient ischemic attack (TIA) or cerebrovascular accident (CVA). **Results.** The analysis showed that models composed of both morphological and haemodynamic factors were better predictors of TIA/CVA compared with models based on either morphological or haemodynamic factors separately. Maximum ostium diameter, length of the centreline, blood flow velocity within the LAA, oscillatory shear index, and time average wall shear stress parameters were found to be key risk factors for TIA/CVA prediction. In addition, TIA/CVA patients presented more flow stagnation within the LAA. **Conclusion.** Thrombus formation in the LAA is the result of multiple factors. Analyses based only on morphological or haemodynamic parameters are not precise enough to predict such a phenomenon, as demonstrated in our results; a better patient stratification can be obtained by jointly analysing morphological and haemodynamic features.

1. Introduction

Atrial fibrillation (AF) is considered the most common of human arrhythmias. Approximately 2% of people younger than age 65 and about 9% of people aged 65 years or more have AF [1]. AF is currently seen as a marker of an increased risk of stroke since it favours thrombus formation inside the left atrium (LA). Around 99% of thrombi in nonvalvular AF are formed in the left atrial appendage (LAA) [2]. LAA

shapes are complex and variable among the general population; researchers have sought to classify LAA morphologies and relate them to the risk of thrombus formation. The most established classification was initially proposed by Wang et al. [3] that classifies the LAA in four shapes: chicken-wing, cauliflower, windsock, and cactus. The authors reported that cauliflower and non-chicken-wing shapes were associated with more risk of thrombus formation [4]. Recently, another classification system [5] has

been proposed based on the LAA angulation (LAA-H/L), defining as low-risk morphology (LAA-L) the ones with an acute angle bend or fold from the middle and proximal part of the LAA, and high-risk (LAA-H) otherwise. However, none of these classifications have achieved a scientific consensus due to their qualitative interpretation [6]. More quantitative anatomical factors based on the LAA orifice/ostium (interface between LA and LAA) such as its area, volume, minimum/maximum diameter, and irregularity, as well as LAA volume, width, and height, among others, have also been used for thrombogenic risk and stroke subtype stratification [7, 8].

At the same time, blood flow haemodynamics is a factor to consider for the assessment of the risk of thrombus formation, following Virchow's triad principles [9]. Low velocities and stagnated flow have been associated with the triggering of the inflammatory process and therefore the risk of thrombus generation [10, 11]. However, on daily clinical practice, LA haemodynamics can only be studied using echocardiography images, usually simplified to a single blood flow velocity value at one point in space and in time (e.g., centre of LAA ostium at end-diastole) [12]. Advanced imaging techniques such as 4D flow magnetic resonance imaging (MRI), allowing a more complete blood flow analysis, are emerging, but they still provide limited information in the left atria [11]. At this juncture, patient-specific models (e.g., digital twin concept [13]) based on computational fluid dynamics can provide a better haemodynamic characterization of the LA and LAA, deriving in silico indices describing blood flow at each point of the geometry over time. In the last decade, there have been several attempts to develop fluid simulation frameworks for the blood flow analysis of the human LA and LAA [14–16], but they have only been applied to a very limited number of patient-specific cases, except in a recent study with a cohort of simulated patients above fifty [17].

The aim of our study was to perform a joint analysis of morphological and in silico haemodynamic parameters from 30 patient-specific cases with and without history of transient ischemic attack (TIA) or cerebrovascular accident (CVA), to identify the combination of parameters that better predict TIA/CVA, as a potential surrogate of risk of thrombus formation and stroke.

2. Materials and Methods

2.1. Clinical Data. The initial patient cohort consisted of a total of 83 patients with AF from OLV Hospital in Aalst, Belgium. Nonvalvular patients ($n=71$) were split into two groups based on whether or not they had suffered TIA/CVA; patients with valvular AF ($n=12$) were discarded. All patients from our study underwent radiofrequency ablation of the pulmonary veins and were on permanent anticoagulation and gave written informed consent. The 3D LA models were acquired by reconstructing 3D rotational angiography images (3DRAs) obtained using an Innova 3D system (GE Healthcare, Chalfont St Giles, UK) and reconstructed into isotropic 3D volumes through the scanner workstation, providing isotropic 3D images with

0.23 mm or 0.45 mm volumetric pixel size for 512 or 256 pixels per dimension, respectively [18]. Segmentation of the left atria was achieved with semiautomatic thresholding and region-growing algorithms available at the scanner console.

Morphological parameters were extracted from all nonvalvular patients. However, based on the quality of acquisitions, in silico simulations were only run on 30 patients (15 with history of TIA/CVA and 15 without), as shown in Figure 1(a). The available clinical data included weight, age, body mass index (BMI), body shape area (BSA), and the LAA morphology type (e.g., chicken-wing, cactus, windsock, or cauliflower, labelled by experts). The type of AF was also included, employing a distinction between paroxysmal or persistent (if lasting a maximum of 7 days or longer, respectively). The CHA2DS2-VASc score was assigned assuming that TIA/CVA cases had no history of thrombus before grading, which means that a high value of the score depends on other factors considered by the method. Mitral valve insufficiency was defined according to the angiographic grading and CHA2DS2-VASc score. A detailed breakdown of the steps followed in our study, including the advanced statistical classification, is shown in Figure 1(b).

2.2. Morphological Indices. Before the automatic morphological characterization of the LAAs, a common reference system was defined for all LAAs by aligning the ostium plane with the zx -plane. The following were the analysed LAA morphological parameters (see Figure 2): the LAA volume and area; the neck height (h_{LAA}), the distal point length (h_{θ}), the LAA anterior and posterior distances (d_A and d_P , respectively in Figure 2) between the LAA centre of mass (p_{mass}) and the most distal points in the x direction, as well as its sum (anterior-posterior distance, d_{AP}); the LAA centreline, using the VIDAA software [19]; and LAA tortuosity (η_{LAA}). Additionally, the LAA ostium was characterized by its maximum and minimum diameters (D_{max} and D_{min} , respectively) and its area and perimeter. Figure 2 shows a graphical representation of the estimated morphological parameters. Further details on the computation of morphological parameters are given in Supplementary Table S1 (see Figure S.1).

2.3. In Silico Haemodynamic Indices. Computational fluid dynamics (CFD) simulations with dynamic mesh movement of the mitral valve (MV) annulus ring were carried out by using ANSYS Fluent Solver 19.2 (Ansys, Inc., Pennsylvania, USA). In our study, we applied the boundary conditions (BCs) proposed by Mill et al. [20, 21]. They were defined as pressure inlet at the pulmonary veins (PVs) and as velocity outlet at the MV. A pressure waveform was extracted from one patient with AF in sinus rhythm through catheterization, while the velocity profile was extracted from a Doppler echocardiography acquisition; both conditions were applied to all simulated cases. Complete details on the 3D model construction and in silico simulation set-up are given in Supplementary Table S2 (see Figure S.2)

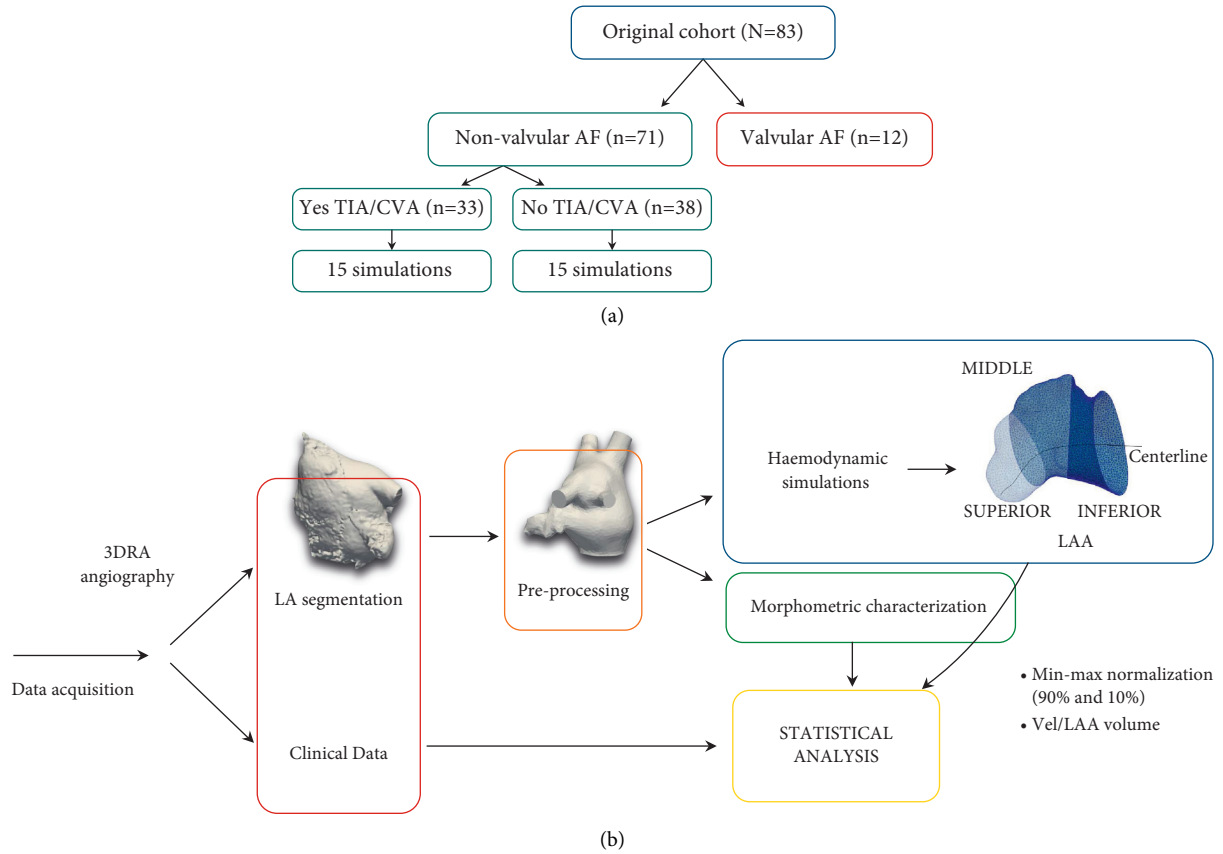


FIGURE 1: (a) Organization of the cohort of patients with atrial fibrillation (AF), transient ischemic attack (TIA), and cerebrovascular accident (CVA). (b) Computational pipeline followed in the study: data acquisition, left atrium (LA) segmentation from medical images, preprocessing, morphologic characterization of the LA and left atrial appendage (LAA), haemodynamic simulations, postprocessing, and statistical analysis of the data.

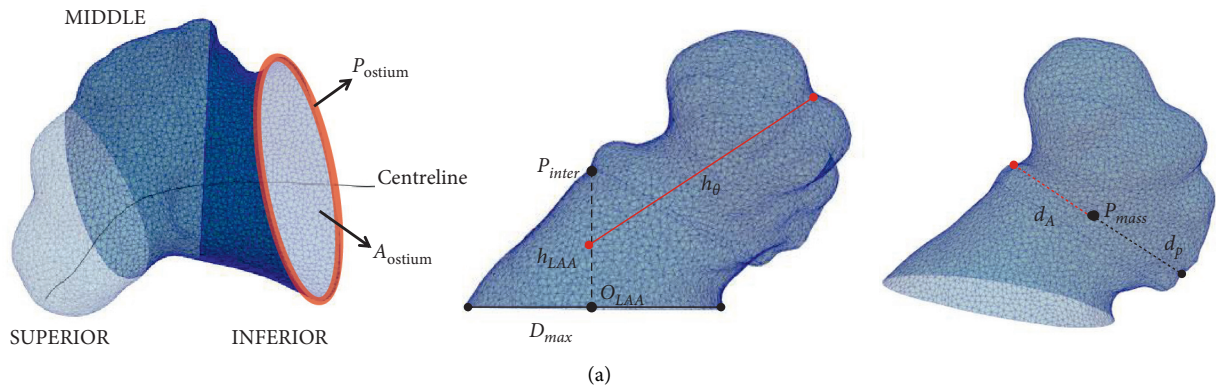


FIGURE 2: Continued.

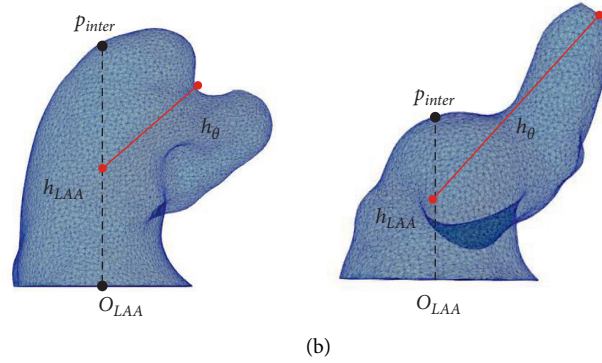


FIGURE 2: (a) Left atrial appendage division in three regions for the haemodynamic analysis (left) and morphological indices: ostium perimeter (p_{ostium}) and area (A_{ostium}), neck height (h_{LAA}), distal point length (h_{θ}), maximum ostium diameter (D_{max}), origin of the LAA (O_{LAA}), intersected point (p_{inter}), anterior (d_A) and posterior (d_P) distance of the LAA and LAA, and centre of mass (p_{mass}). (b) Examples of LAA with high and low tortuosity (left and right, respectively).

Haemodynamic indices from fluid simulations such as blood flow velocities were estimated averaging values of the second and third simulated beats (including systolic and diastolic phases) since the first one was used to stabilize the simulations. The time average wall shear stress (TAWSS), oscillatory shear index (OSI), relative residence time (RRT), and endothelial cell activation potential (ECAP; ratio between OSI and TAWSS (Equations (1)–(3)), with high values corresponding to low velocities and high flow complexity) were computed from the wall shear stress (WSS) at the LAA wall in order to identify the areas with high thrombogenic risk [22]. Finally, blood flow stagnation inside the LAA was assessed by integrating the flow rate at the ostium.

$$TAWSS = \frac{1}{T} \int_0^T |WSS| dt, \quad (1)$$

$$OSI = \frac{1}{2} \frac{\int_0^T WSS dt}{\int_0^T |WSS| dt}, \quad (2)$$

$$ECAP = \frac{OSI}{TAWSS}, \quad (3)$$

$$RRT = [1 - (2 \cdot OSI) \cdot TAWSS]^{-1}. \quad (4)$$

Furthermore, a local analysis was also performed by dividing each LAA into three regions (see Figure 2): inferior (closest to the ostium), middle, and superior (farthest to the ostium). The LAA regional division was achieved by dividing the LAA centreline into three parts. The analysis of morphological and haemodynamic parameters was performed comparing control cases versus TIA/CVA, as well as chicken-wing versus non-chicken-wing LAA morphologies.

2.4. Statistical Analysis. The statistical analysis was performed using R Studio 1.2.1335 and can be divided into two main blocks: exploratory analysis and inferential analysis. Results are presented in terms of median (minimum–maximum) for continuous and non-normally

distributed variables and mean \pm standard deviation (SD) for continuous and normally distributed variables, whilst categorical data as characterized as count (percentage). Student's t -test, Mann-Whitney–Wilcoxon and X^2 tests were used depending on the nature of the variable studied. The level of significance (α) was set to 0.05. Relevant parameters in terms of significant differences (p value < 0.05) were considered potential risk factors. Afterwards, a stepwise regression model with only those morphological parameters that were statistically significant in the aforementioned statistical analysis was performed. For these stepwise regression models, the Akaike information criterion (AIC) [23] was used to study their prediction accuracy. A lower AIC represents a smaller information loss by the model, so the smaller the AIC, the higher the quality of the model. The output of the best morphology-based model was combined with the haemodynamic parameters to perform a joint analysis. Moreover, machine learning algorithms such as random forest were implemented to corroborate which parameters might play a critical role to classify cases in controls and TIA/CVA, as a complement to the classical statistical tests and regression models. The input for the random forest was the morphological parameters (LAA and LA volume, ratio LAA_v/LA_v , length of the centreline, LAA height, ostium anterior distance, maximum ostium diameter, ostium area, and LAA shape) found in the literature that contribute in the process of thrombus formation [4, 24–26], together with haemodynamic ones (ECAP, OSI, RRT, TAWSS, and velocity). Relevance parameters were obtained finding the best hyperparameters with a grid search procedure (number of trees = 500, variables sampled at each split = 4, maximum number of terminal nodes = 90). The Gini index was used to assess the importance of each predictor.

For the haemodynamic indices (ECAP, TAWSS, OSI, and RRT), the data were normalized applying a minimum–maximum sampling approach in all the studies. Percentiles 90% and 10% were discarded to be robust against outliers while analysing the whole LAA and its

regions. For the blood flow velocity within the LAA, data were normalized by the total volume of the LAA in each case.

3. Results

3.1. Clinical and Morphological Analysis. No significant differences were found in AF persistent vs. paroxysmal cases ($p=1.00$) between the TIA/CVA and control groups. On the same line, the prevalence of mitral insufficiency and the CHA2DS2-VASc score did not show significant differences ($p=0.832$ and $p=0.343$, respectively). The differences between both groups of patients were minimal, as can be seen in Table 1.

On the other hand, as detailed in Table 2, significant differences between TIA/CVA and control groups were found in morphological parameters such as the maximum ($p<0.001$), minimum ($p=0.01$), and mean ($p=0.001$) diameters of the ostium, as well as its minimum radius ($p=0.02$). The length of the LAA centreline was also significant ($p=0.05$), as well as all ostium diameters, being larger in the TIA/CVA group. The LAA width, together with the anterior and anterior-posterior (AP) distances also showed significant levels ($p=0.01$ and $p=0.02$, respectively). The LAA shape was not significantly different between controls and TIA/CVA neither when classifying the LAA in chicken-wing versus non-chicken-wing (which were the majority of cases, 86%) nor in the classical four LAA types. Three TIA/CVA cases for the shape analysis were discarded due to the low quality of the reconstructed models and thus unclear shape. Morphological parameters obtained in the subset of cases where fluid simulations were run (see S3, Table S.3) showed the same trends, but fewer of them (maximum ostium diameters, ostium eccentricity, centreline length, and tortuosity) were statistically significant. The results of the regression model only including significant morphological parameters in the whole set of controls and TIA/CVA cases showed that the maximum ostium diameter, perimeter and area of the ostium, anterior distance, LAA area, and centreline length were the ones better differentiating TIA/CVA from control cases. However, the AIC obtained in morphology-based models was high among all the other ones (AIC = 85.96), thus on the lower range of accuracy.

3.2. Haemodynamic Analysis. Figure 3 shows three-dimensional maps of ECAP of two exemplary TIA/CVA and control cases, in which the highest ECAP values (red areas in the figure) are located in the LAA regions in both cases. Lower blood flow velocities in the whole LAA were estimated in the TIA/CVA group compared with controls, as summarised in Table 3. In addition, higher ECAP, OSI, and RRT, all indicators of a higher risk of thrombus formation, were found in the TIA/CVA group. The TIA/CVA group also presented a worse flow washout from the LAA, indicating a higher percentage of stagnated blood in comparison with the control group (19.77% vs. 12.39%, respectively). Despite these trends, differences were not statistically significant between controls and TIA/CVA groups for any of the estimated haemodynamic indices. In all patients, vortex structures were visually present, but no substantial

qualitative differences were found in terms of vorticity between TIA/CVA and control groups.

Analysing the LAA geometry per regions, blood flow velocities progressively decreased from the ostium to the superior part of the LAA (i.e., closer to the LAA tip) for both groups, still with higher values for controls. Conversely, haemodynamic indices were higher in the superior region for both groups, with larger differences between them.

Table 4 shows the *in silico* haemodynamic indices for each region of the LAA for chicken-wing and non-chicken-wing patients. Higher blood flow velocities, statistically significant ($p=0.04$), were obtained for the chicken-wing group vs. the non-chicken-wing cases, consistently decreasing from the ostium to the superior LAA region. On the other hand, most of the remaining haemodynamic indicators of thrombogenic risk (ECAP, OSI, RRT) were higher in the chicken-wing group, led by large differences in the superior part of the LAA.

3.3. Joint Analysis of Morphological and Haemodynamic Parameters. The joint analysis reported that the most significant morphological indices (e.g., ostium characteristics, LAA area, and centreline length) were always good predictors of TIA/CVA. However, when *in silico* haemodynamic indices were added to the analysis, the results substantially improved the AIC metric obtained with morphological indices alone. A model with an AIC of 14 was obtained when adding haemodynamic indices (versus 85.96 with only morphological ones) such as RRT and TAWSS, along with some morphological indices (LAA volume, ostium area, anterior distance, and length of the centreline) that were reported as potential indicators of TIA/CVA history. The most distinguished features used for the region partition of each tree in the random forest were similar to those factors found in the previous statistical analysis. As can be seen in Figure 4, the maximum ostium diameter, OSI (i.e., flow complexity), and the length of the centreline were reported as good candidates to be predictors of thrombus formation among others. Analysing the model, the classification accuracy achieved was 70%.

4. Discussion

In this study, we assessed the significance of parameters characterizing the LAA morphology and haemodynamics to distinguish TIA/CVA from control cases. Factors representing Virchow's triad such as stasis, changes in the atrial geometry, specific LAA morphologies, and unfavourable haemostatic milieu are all likely to contribute to thrombus formation and thereby stroke risk [27].

Nevertheless, currently there is not any robust approach in AF patients to predict the risk of events potentially leading to stroke such as TIA/CVA or thrombus formation. Despite being regularly used, it has been proven that scores such as the CHA2DS2-VASc are not fully reliable, with some patients having low score values still generating thrombus [28]; the CHA2DS2-VASc resulted to be not significant in our study. Characterizing LA/LAA morphology with qualitative,

TABLE 1: Clinical features of patients with and without a history of TIA/CVA

Characteristics	Control (<i>n</i> = 38)	TIA/CVA (<i>n</i> = 33)	<i>p</i> value
Age (years)	62.6 ± 8.9	67.2 ± 9.4	0.035
BMI (kg/m ²)	28.4 ± 4.6	26.5 ± 4.8	0.097
BSA (m ²)	2.0 ± 0.25	2.0 ± 0.25	0.589
Weight (kg)	86.4 ± 15.9	78.5 ± 16.6	0.045
<i>Gender</i>			
Female	11 (28.9%)	19 (57.6%)	0.019
Male	27 (71.1%)	14 (42.4%)	
<i>AF type</i>			
Paroxysmal	25 (65.8%)	21.0 (63.6%)	1.000
Persistent	13 (34.2%)	12 (36.4%)	
<i>CHA2DS2-VASc*</i>			
0	9 (23.7%)	5 (15.2%)	0.343
1	9 (23.7%)	5 (15.2%)	
≥2	20 (52.6%)	23 (69.7%)	
<i>Mitral insufficiency</i>			
No	20 (52.6%)	15 (45.5%)	0.832
Grade 1	15 (39.5%)	14 (42.4%)	
Grade 2	3 (7.9%)	4 (12.1%)	

BMI = body mass index, BSA = body shape area, CVA = cerebrovascular accident, TIA = transient ischemic attack. Results are presented as mean ± SD or *n* (%). *Current TIA/CVA excluded.

TABLE 2: Volumetric and morphological features of patients with and without history of TIA/CVA.

Characteristics	Control (<i>n</i> = 38)	TIA/CVA (<i>n</i> = 33)	<i>p</i> value
Max. ostium diameter (mm)	25.77 ± 4.40	30.20 ± 4.90	<0.001
Min. ostium diameter (mm)	17.46 ± 3.66	19.63 ± 2.95	0.01
Mean ostium diameter (mm)	21.62 ± 3.70	24.91 ± 3.66	0.001
Min. ostium radius (mm)	6.99 ± 2.37	8.20 ± 1.81	0.02
Ostium area (mm ²)	367.18 ± 125.16	486.35 ± 148.42	<0.001
Ostium perimeter (mm)	71.16 ± 12.27	80.99 ± 12.14	0.001
Eccentricity	0.32 ± 0.10	0.34 ± 0.08	0.24
LAA height (mm)	14.80 (9.18–22.93)	15.34 (8.83–30.63)	0.25
Length of the centreline (mm)	34.48 ± 7.06	38.82 ± 8.74	0.05
Tortuosity of the centreline	0.79 (0.50–0.96)	0.77 (0.45–0.88)	0.36
LAA anterior distance (mm)	13.87 ± 3.75	16.03 ± 3.18	0.01
LAA posterior distance (mm)	11.38 ± 3.17	12.83 ± 3.54	0.08
LAA anterior-posterior distance (mm)	25.26 ± 6.70	28.86 ± 6.38	0.02
Bending (degrees)	114 ± 17.55	103 ± 23.84	0.07
Atrium volume (ml)	163 (82–256)	164 (100–269)	0.94
LAA area (mm ²)	2225 (1183–3918)	2677 (1747–6006)	0.03
LAA volume (ml)	6.63 (2.59–15.50)	8.09 (4.12–15.88)	0.02
<i>LAA shape*</i>			
(i) Chicken-wing	6 (15.79%)	4 (13.33%)	0.53
(ii) Non-chicken-wing	32 (84.21%)	26 (86.67%)	0.45
<i>LAA shape*</i>			
(i) Chicken-wing	6 (15.79%)	4 (13.33%)	0.53
(ii) Cauliflowers	10 (26.32%)	8 (26.67%)	0.82
(iii) Cactus	13 (34.21%)	7 (23.33%)	0.26
(iv) Windsock	9 (23.68%)	11 (36.67%)	0.82

AP = anterior-posterior; CVA = cerebrovascular accident; Max = maximum; Min = minimum; TIA = transient ischemic attack. *Data were unclear for 3 TIA/CVA cases. Results were presented as mean ± SD or median (min–max) or *n* (%).

subjective, or too simple parameters is also insufficient to capture the high complexity and large variability of LAA shapes. The classical LAA morphology type classification (e.g., chicken-wing, etc.) is not rigorous enough (i.e., high interobserver

variability), leading to confronted results [6, 29, 30] when related to the risk of thrombus formation. In the studied database, we did not find differences in the percentage of chicken-wing LAA morphologies in controls and TIA/CVA groups,

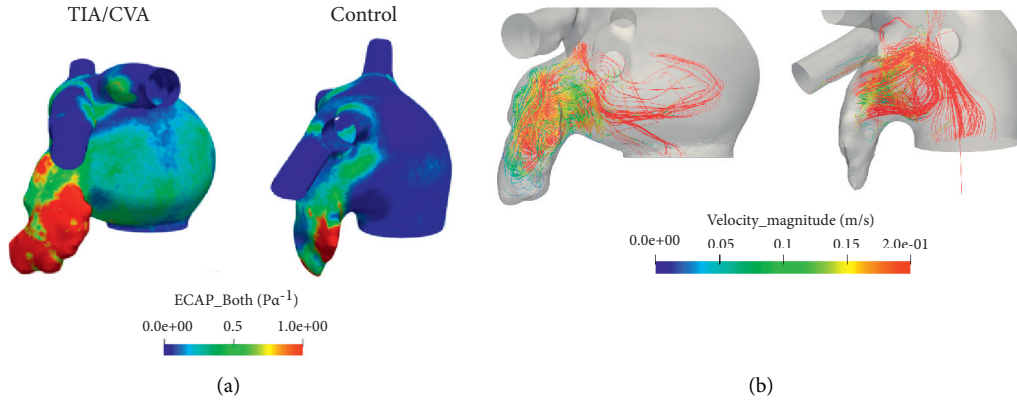


FIGURE 3: (a) Three-dimensional maps of endothelial cell activation potential (ECAP) for a transient ischemic attack or cerebrovascular accident patient (left) and a control case (right). High ECAP values (red areas) indicate a higher risk of thrombus formation due to low velocities and complex blood flow. (b) These velocities as well as the complexity of the flow within the LAA can be visualized with the streamlines for a thrombus case (left), while in a control case (right) flow remains in the ostium and does not reach the tip part of the LAA.

TABLE 3: Haemodynamic indices (mean \pm standard deviation) for the whole LAA in controls and TIA/CVA groups.

	Control	TIA/CVA	<i>p</i> value
TAWSS (Pa)	0.31 \pm 0.12	0.35 \pm 0.14	0.40
ECAP (1/Pa)	0.87 \pm 0.61	1.08 \pm 0.69	0.35
OSI	0.15 \pm 0.05	0.17 \pm 0.04	0.17
RRT (s)	10.03 \pm 5.97	11.38 \pm 7.04	0.62
Vel/LAAv (m-ml/s/ml)	0.99 \pm 0.80	0.84 \pm 0.35	0.93

CVA = cerebrovascular accident; ECAP = endothelial cell activation potential; LAAv = left atrial appendage volume; OSI = oscillatory shear index; RRT = relative resident time; TAWSS = time average wall shear stress; TIA = transient ischemic attack; Vel = velocity. Higher values of ECAP, OSI, and RRT as well as lower values of TAWSS and Vel/LAAv indicate a higher risk of thrombus formation.

TABLE 4: Haemodynamic indices (mean \pm standard deviation) for the whole LAA and each region for chicken-wing (CW) and non-chicken-wing (Non-CW) LAA shapes.

	Inferior		Middle		Superior		Whole	
	Non-CW	CW	Non-CW	CW	Non-CW	CW	Non-CW	CW
TAWSS (Pa)	0.51 \pm 0.22	0.50 \pm 0.14	0.26 \pm 0.13	0.23 \pm 0.09	0.11 \pm 0.08	0.11 \pm 0.10	0.33 \pm 0.14	0.33 \pm 0.07
ECAP (1/Pa)	0.48 \pm 0.22	0.47 \pm 0.20	1.11 \pm 0.86	0.96 \pm 0.47	4.30 \pm 6.13	5.67 \pm 5.12	0.92 \pm 0.61	1.17 \pm 0.80
OSI	0.16 \pm 0.05	0.17 \pm 0.06	0.14 \pm 0.06	0.14 \pm 0.06	0.12 \pm 0.05	0.14 \pm 0.04	0.16 \pm 0.05	0.17 \pm 0.06
RRT (s)	4.96 \pm 2.02	4.82 \pm 1.56	12.52 \pm 8.52	11.22 \pm 5.42	49.88 \pm 61.59	68.51 \pm 59.17	10.23 \pm 6.32	12.25 \pm 7.12
Vel/LAAv (m-ml/s)	1.18 \pm 0.83	1.47 \pm 0.32	0.50 \pm 0.43	0.67 \pm 0.17	0.25 \pm 0.30	0.29 \pm 0.25	0.85 \pm 0.67	1.11 \pm 0.26

CW = chicken-wing; ECAP = endothelial cell activation potential; LAAv = left atrial appendage volume; OSI = oscillatory shear index; RRT = relative resident time; TAWSS = time average wall shear stress; TIA = transient ischemic attack; Vel = velocity. Results with statistical differences are in bold. Higher values of ECAP, OSI and RRT as well as lower values of TAWSS and Vel/LAAv indicate a higher risk of thrombus formation.

disagreeing with di Biase et al. [4] findings (e.g., less likelihood of an embolic event for chicken-wing LAA morphologies). Nevertheless, our models were extracted from angiography images that have a low resolution, and thus a precise assessment of the LAA shape might not be possible. In addition, when introducing the variable shape in our random forest, its importance was minimal.

On the other hand, other volumetric and morphological parameters such as ostium measurements (i.e., diameters, radius, area, perimeter), the LAA area/volume, and the centreline length were found to be good predictors of TIA/CVA events, in agreement with other studies [24, 25], suggesting a higher risk for larger LAA and ostium.

However, Khurram et al. [29] found smaller LAA and ostium being more associated with lower thrombogenic risk. In our study, despite combining multiple clinical data and morphological parameters, the statistical studies produced regression models with limited accuracy, represented as high AIC metric values. As a direct consequence of this inaccuracy, the obtained parameters as potential risk factors might be unreliable.

The *in silico* haemodynamic indices resulting from our simulations showed trends in agreement with literature [4], i.e., TIA/CVA cases being associated with lower blood flow velocities, more complex patterns, larger residence times, and worse flow washout than controls. Nevertheless, all simulations

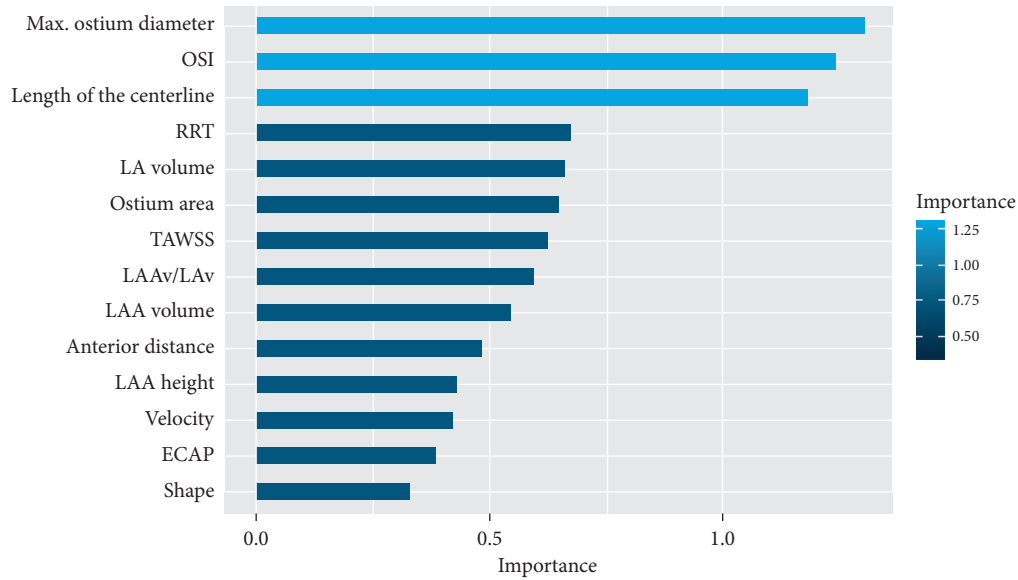


FIGURE 4: Model of the random forest performance in terms of Gini index. OSI: oscillatory shear index; RRT: relative residence time; LAAv: left atrial appendage volume; LAv: left atrium volume; TAWSS: time average wall shear stress; ECAP: endothelial cell activation potential.

were run with the same generic boundary conditions, which prevented more personalised outcomes that could be obtained with patient-specific boundary conditions (e.g., mitral valve velocity profile from Doppler studies). Additionally, differences were not statistically significant due to the large variability in each cohort (see standard deviations in Table 3) and the small number of cases where simulations could be run. In addition to the patient-specific boundary conditions, it could be interesting to study the effect of anticoagulation treatment on thromboembolic events in long term using *in silico* models.

When comparing chicken-wing vs. non-chicken-wing LAA morphologies, the latter presented lower blood flow velocities over the whole LAA, with statistical significance, in concordance to research assigning a protective role towards thrombus formation to chicken-wing LAA [4]. However, the regional analysis showed that the remaining haemodynamic indices were higher (i.e., more risk of thrombus formation) in the superior part of the LAA in chicken-wing morphologies, due to their particular elongated shape favouring complex flows and stagnation.

The joint analysis of morphological and haemodynamic indices achieved a better fitted predictive model than when analysed separately, with a substantial reduction of the AIC metric (from 85.96 with only morphological parameters to 14 when adding optimal haemodynamic indices). The model was obtained combining morphological features characterizing ostium and LAA size (e.g., the maximum ostium diameter, LAA area, and centreline length) together with haemodynamic indices of the whole LAA, mainly representing blood flow velocity magnitude (e.g., TAWSS and Vel/LAAv values). The results of the random forest algorithm reported that the maximum ostium diameter, OSI, and length of the centreline could be potential predictors of thrombogenic risk.

The present study demonstrates the benefit of using quantitative descriptors of blood flow patterns in the LA for the

prediction of thrombogenic risk. However, obtaining *in-vivo* patient-specific data to fully characterize the 4D nature of LA/LAA haemodynamics is not yet possible in clinical routine. Computational simulations and digital twin models [13] offer an interesting alternative to derive *in silico* indices to be combined with morphological parameters from medical images for a personalised estimation of thrombogenic risk for a given patient. However, access to good-quality imaging data to build 3D models (e.g., geometry and boundary conditions) is not easy. Moreover, the whole fluid modelling pipeline is usually computationally demanding, requiring access to advanced hardware infrastructures and including tedious manual steps, preventing the processing of large amounts of cases. Nevertheless, we developed a modelling pipeline [19] to generate geometry-specific simulations in one working day.

This study has focused on studying the influence of LA/LAA morphology and *in silico* haemodynamics on thrombus formation before the implantation of a LAAO device, which can lead to a better patient selection and personalised therapy choice. However, the developed modelling pipeline to create haemodynamics simulations has also shown [17–21] to be useful in determining the formation of thrombus after the implantation of LAAO devices (i.e., device-related thrombus). Unfortunately, the required follow-up data to perform such verification were not available in the analysed patients in this study.

Some limitations of this study should be taken into consideration. First, the analysed cases were divided according to TIA/CVA history, which does not necessarily involve thrombus formation or degradation to stroke. In addition, we did not know if the TIA/CVA had its origin in the LAA. Moreover, the available imaging data were acquired with a 3DRA system, which has lower spatial resolution than computerized tomography (CT) scans and prevented the building of *in silico* simulations for all the available cases. The drawback of the 3DRA is

that the obtained image quality highly depends on factors such as contrast injection. However, 3DRA with the use of contrast offers a reconstruction of the left atrial geometry in a more precise way (easily segmented with simple image processing tools) than 3D echocardiographic images, which is key to build computational models and run fluid simulations. Our study emphasises the significance of having patient-specific data as boundary conditions, e.g., from Doppler echocardiography, for having more realistic fluid simulations; as they were not available in the analysed cohort, some haemodynamic indices were not significantly different between TIA/CVA and control cases.

5. Conclusions

Thrombus formation in the LAA, potentially leading to transient ischemic attacks, cerebrovascular accidents, and stroke, results from the combination of different factors, including morphology and haemodynamics. However, their independent analysis does not offer the necessary holistic view to properly understand the underlying pathophysiological mechanisms and to estimate thrombogenic risk on an individual basis. We demonstrate in our study that the joint analysis of morphological parameters and in silico haemodynamic indices provides a better stratification of patients with and without TIA/CVA history. Relevant factors included the maximum ostium diameter and centreline length as well as in silico haemodynamic indices capturing blood flow complexity and magnitude values. The TIA/CVA group was associated with larger LAA and ostium as well as with lower blood flow velocities and more complex flow patterns, as assessed by various in silico haemodynamic indices. Furthermore, chicken-wing LAA morphologies presented higher blood velocities than non-chicken-wing ones.[31–34]

Abbreviations

AF:	Atrial fibrillation
BCs:	Boundary conditions
CFD:	Computational fluid dynamics
CVA:	Cerebrovascular accident
ECAP:	Endothelial cell activation potential
LA:	Left atrium
LAA:	Left atrial appendage
MV:	Mitral valve
OSI:	Oscillatory shear stress
PVs:	Pulmonary veins
RRT:	Relative residence time
TAWSS:	Time average wall shear stress
TIA:	Transient ischemic attack.

Data Availability

The computational fluid dynamic models, morphological database, haemodynamic database, and R studio script files data used to support the findings of this study are available from the corresponding author upon request.

Conflicts of Interest

The authors declare that there are no conflicts of interest regarding the publication of this paper.

Acknowledgments

This work was supported by the Spanish Ministry of Science, Innovation and Universities under the Retos I+D Programme (RTI2018-101193-B-I00), the Maria de Maeztu Units of Excellence Programme (MDM-2015-0502), the Spanish Ministry of Economy and Competitiveness under the Programme for the Formation of Doctors (PRE2018-084062), and MINECO (RYC-2015-18888).

Supplementary Materials

In Supplementary Materials, a description of the computation of the morphological parameters studied, as well as examples of LAA morphologies studied (S1) is presented. In addition, the pipeline followed to perform the 3D model construction of the LA geometries and the set-up of the in silico simulations (S2); and finally, the results of the statistical analysis of all the volumetric and morphological parameters of the cases simulated (S3). (*Supplementary Materials*)

References

- [1] F. Rahman, G. F. Kwan, and E. J. Benjamin, “Global epidemiology of atrial fibrillation,” *Nature Reviews Cardiology*, vol. 11, no. 11, pp. 639–654, 2014.
- [2] A. Cresti, M. A. García-Fernández, H. Sievert et al., “Prevalence of extra-appendage thrombosis in non-valvular atrial fibrillation and atrial flutter in patients undergoing cardioversion: a large transoesophageal echo study,” *Euro-Intervention*, vol. 15, no. 3, pp. e225–e230, 2019.
- [3] Y. Wang, L. di Biase, R. P. Horton, T. Nguyen, P. Morhanty, and A. Natale, “Left atrial appendage studied by computed tomography to help planning for appendage closure device placement,” *Journal of Cardiovascular Electrophysiology*, vol. 21, no. 9, pp. 973–982, 2010.
- [4] L. di Biase, P. Santangeli, M. Anselmino et al., “Does the left atrial appendage morphology correlate with the risk of stroke in patients with atrial fibrillation?” *Journal of the American College of Cardiology*, vol. 60, no. 6, pp. 531–538, 2012.
- [5] S. Yaghi, A. D. Chang, R. Akiki et al., “The left atrial appendage morphology is associated with embolic stroke subtypes using a simple classification system: a proof of concept study,” *Journal of Cardiovascular Computed Tomography*, vol. 14, no. 1, pp. 27–33, 2020.
- [6] L. Wu, E. Liang, S. Fan et al., “Relation of left atrial appendage morphology determined by computed tomography to prior stroke or to increased risk of stroke in patients with atrial fibrillation,” *The American Journal of Cardiology*, vol. 123, no. 8, pp. 1283–1286, 2019.
- [7] W. K. Jeong, J.-H. Choi, J. P. Son et al., “Volume and morphology of left atrial appendage as determinants of stroke subtype in patients with atrial fibrillation,” *Heart Rhythm*, vol. 13, no. 4, pp. 820–827, 2016.
- [8] A. C. Boyd, T. McKay, S. Nasibi, D. A. B. Richards, and L. Thomas, “Left ventricular mass predicts left atrial

- appendage thrombus in persistent atrial fibrillation,” *European Heart Journal-Cardiovascular Imaging*, vol. 14, no. 3, pp. 269–275, 2013.
- [9] T. Watson, E. Shantsila, and G. Y. Lip, “Mechanisms of thrombogenesis in atrial fibrillation: virchow’s triad revisited,” *The Lancet*, vol. 373, no. 9658, pp. 155–166, 2009.
- [10] A. Naser and A. Ke, “Left atrial blood stasis and von willebrand factor-ADAMTS13 homeostasis in atrial fibrillation,” *Arteriosclerosis, Thrombosis, and Vascular Biology*, vol. 31, no. 11, pp. 2760–2766, 2011.
- [11] M. Markl, D. C. Lee, and M. L. Carr, “Assessment of left atrial and left atrial appendage flow and stasis in atrial fibrillation,” *Journal of Cardiovascular Magnetic Resonance*, vol. 17, no. 1, p. M3, 2015.
- [12] R. Beigel, N. C. Wunderlich, S. Y. Ho, R. Arsanjani, and R. J. Siegel, “The left atrial appendage: anatomy, function, and noninvasive evaluation,” *Journal of the American College of Cardiology: Cardiovascular Imaging*, vol. 7, no. 12, pp. 1251–1265, 2014.
- [13] J. Corral-Acero, F. Margara, and M. Marciniak, “The “digital twin” to enable the vision of precision cardiology,” *European Heart Journal*, vol. 41, 2020.
- [14] T. Otani, A. Al-Issa, A. Pourmorteza, E. R. McVeigh, S. Wada, and H. Ashikaga, “A computational framework for personalized blood flow analysis in the human left atrium,” *Annals of Biomedical Engineering*, vol. 44, no. 11, pp. 3284–3294, 2016.
- [15] A. Masci, L. Barone, and L. Dedè, “The impact of left atrium appendage morphology on stroke risk assessment in atrial fibrillation: a computational fluid dynamics study,” *Frontiers in Physiology*, vol. 9, 2019.
- [16] M. Garcia-Villalba, L. Rossini, and A. Gonzalo, “Demonstration of patient-specific simulations to assess left atrial appendage thrombogenesis risk,” *Frontiers in Physiology*, vol. 12, Article ID 596596, 2021.
- [17] J. Mill, J. Harrison, B. Legghe et al., “In-silico analysis of the influence of pulmonary vein configuration on left atrial haemodynamics and thrombus formation in a large cohort,” in *Functional Imaging and Modeling of the Heart*, D. B. Ennis, L. E. Perotti, and V. Y. Wang, Eds., , pp. 605–616, Springer International Publishing, 2021.
- [18] A. L. Olivares, E. Silva, M. Nuñez-Garcia et al., “In silico analysis of haemodynamics in patient-specific left atria with different appendage morphologies,” *Functional Imaging and Modelling of the Heart*, vol. 10263, pp. 412–420, 2017.
- [19] A. M. Aguado, A. L. Olivares, C. Yagüe et al., “In silico optimization of left atrial appendage Occluder implantation using interactive and modeling tools,” *Frontiers in Physiology*, vol. 10, p. 237, 2019.
- [20] J. Mill, V. Agudelo, and C. Hion Li, “Patient-specific flow simulation analysis to predict device-related thrombosis in left atrial appendage occluders,” *Revista Espanola de Cardiologia: Interventional Cardiology (English Edition)*, vol. 3, 2021.
- [21] J. Mill, V. Agudelo, A. L. Olivares et al., “Sensitivity analysis of in silico fluid simulations to predict thrombus formation after left atrial appendage occlusion,” *Mathematics*, vol. 9, no. 18, p. 2304, 2021.
- [22] P. Di Achille, G. Tellides, C. A. Figueroa, and J. D. Humphrey, “A haemodynamic predictor of intraluminal thrombus formation in abdominal aortic aneurysms,” *Proceedings of the Royal Society A: Mathematical, Physical & Engineering Sciences*, p. 470, 2014.
- [23] H. Akaike, “A new look at the statistical model identification,” *IEEE Transactions on Automatic Control*, vol. 19, no. 6, pp. 716–723, 1974.
- [24] J. M. Lee, J.-B. Kim, J.-S. Uhm, H.-N. Pak, M.-H. Lee, and B. Joung, “Additional value of left atrial appendage geometry and hemodynamics when considering anticoagulation strategy in patients with atrial fibrillation with low CHA₂DS₂-VASc scores,” *Heart Rhythm*, vol. 14, no. 9, pp. 1297–1301, 2017.
- [25] J. M. Lee, J. Shim, J.-S. Uhm et al., “Impact of increased orifice size and decreased flow velocity of left atrial appendage on stroke in nonvalvular atrial fibrillation,” *The American Journal of Cardiology*, vol. 113, no. 6, pp. 963–969, 2014.
- [26] M. Taina, R. Vanninen, M. Hedman et al., “Left atrial appendage volume increased in more than half of patients with cryptogenic stroke,” *PLoS One*, vol. 8, no. 11, Article ID e79519, 2013.
- [27] M. Glikson, R. Wolff, G. Hindricks et al., “EHRA/EAPCI expert consensus statement on catheter-based left atrial appendage occlusion-an update,” *EP Europace*, vol. 22, no. 2, p. 184, 2020.
- [28] G. Y. H. Lip, R. Nieuwlaat, R. Pisters, D. A. Lane, and H. J. G. M. Crijns, “Refining clinical risk stratification for predicting stroke and thromboembolism in atrial fibrillation using a novel risk factor-based approach,” *Chest*, vol. 137, no. 2, pp. 263–272, 2010.
- [29] J. He, Z. Fu, L. Yang et al., “The predictive value of a concise classification of left atrial appendage morphology to thrombosis in non-valvular atrial fibrillation patients,” *Clinical Cardiology*, vol. 43, no. 7, pp. 789–795, 2020.
- [30] M. Taina, M. Korhonen, M. Haataja et al., “Morphological and volumetric analysis of left atrial appendage and left atrium: cardiac computed tomography-based reproducibility assessment,” *PLoS One*, vol. 9, no. 7, Article ID e101580, 2014.
- [31] I. M. Khurram, J. Dewire, M. Mager et al., “Relationship between left atrial appendage morphology and stroke in patients with atrial fibrillation,” *Heart Rhythm*, vol. 10, no. 12, pp. 1843–1849, 2013.
- [32] G. Taubin, “Curve and surface smoothing without shrinkage,” in *Proceedings of the IEEE International Conference on Computer Vision*, Cambridge, MA, USA, June 1995.
- [33] M. Evin, F. M. Callaghan, and C. Defrance, “Left atrium MRI 4D-flow in atrial fibrillation: association with la function,” *Computing in Cardiology*, 2015.
- [34] F. Veronesi, C. Corsi, L. Sugeng et al., “Quantification of mitral apparatus dynamics in functional and ischemic mitral regurgitation using real-time 3-dimensional echocardiography,” *Journal of the American Society of Echocardiography*, vol. 21, no. 4, pp. 347–354, 2008.